nature methods

ARTICLES

https://doi.org/10.1038/s41592-019-0651-0

In situ structure determination at nanometer resolution using TYGRESS

Kangkang Song[1,3,5], Zhiguo Shang[1,5], Xiaofeng Fu[1,4,5], Xiaochu Lou[1,5], Nikolaus Grigorieff[2] and Daniela Nicastro[1*]

The resolution of subtomogram averages calculated from cryo-electron tomograms (cryo-ET) of crowded cellular environments is often limited owing to signal loss in, and misalignment of, the subtomograms. By contrast, single-particle cryo-electron microscopy (SP-cryo-EM) routinely reaches near-atomic resolution of isolated complexes. We report a method called 'tomography-guided 3D reconstruction of subcellular structures' (TYGRESS) that is a hybrid of cryo-ET and SP-cryo-EM, and is able to achieve close-to-nanometer resolution of complexes inside crowded cellular environments. TYGRESS combines the advantages of SP-cryo-EM (images with good signal-to-noise ratio and contrast, as well as minimal radiation damage) and subtomogram averaging (three-dimensional alignment of macromolecules in a complex sample). Using TYGRESS, we determined the structure of the intact ciliary axoneme with up to resolution of 12 Å. These results reveal many structural details that were not visible by cryo-ET alone. TYGRESS is generally applicable to cellular complexes that are amenable to subtomogram averaging.

As a result of recent hardware and image-processing advances, SP-cryo-EM can produce three-dimensional (3D) reconstructions of purified native proteins and macromolecular complexes (in sizes ranging from ~50 kDa to several MDa) with near-atomic detail, that is, with a resolution of 3 Å or better[1–4]. Even single-particle cryo-ET of relatively thin (<100 nm) samples containing isolated complexes[5] and of viruses with a high abundance of capsomers[6,7] has reached sub-nanometer resolution. However, relatively thick (>100 nm) and complex cellular samples are not presently amenable to structural study by SP-cryo-EM. The reason being that for unambiguous particle picking and accurate particle alignment, SP-cryo-EM usually requires the particles to be purified, structurally relatively homogeneous, and distributed in a thin monolayer that avoids superposition of particles in the cryo-EM projection images[8].

Unlike other ultrastructural methods, cryo-ET can be used to reconstruct and visualize pleomorphic structures, such as intact cells and organelles in situ, in 3D. In addition, identical repeating components in the reconstructed tomograms, such as axonemal repeats in cilia or chemoreceptors in bacterial membranes, can be resolved in molecular detail using subtomogram averaging, which increases the signal-to-noise ratio and thus the resolution of the reconstruction[9–12]. However, the resolution of cellular cryo-ET and subtomogram averaging is ultimately limited by the need to balance several irreconcilable factors (Supplementary Table 1). For example, a higher electron dose improves the signal-to-noise ratio of the tilt images, increasing accuracy of image alignment and correction of the contrast transfer function (CTF), with positive effects on resolution. On the other hand, a higher electron dose also leads to more structural degradation by radiation damage, limiting useful high-resolution signal to the early exposures in a tomogram. In contrast to thin 'single-particle-type' samples, the signal in tomograms of cellular samples is degraded by: (1) increased inelastic electron scattering owing to the large thickness of cellular samples, with the effective thickness increasing by $1/\cos(\alpha)$ with tilt angle α; (2) incomplete sampling of the reconstruction in Fourier space beyond a given resolution (Crowther criterion: $m = \pi \times D/d$, with number of tilt images m, sample thickness D and resolution d)[13]; (3) beam-induced motion and electrostatic charging affecting images of tilted samples more severely; and (4) the initial fast, and not fully correctable, motion in exposures is reiterated with every new exposure in a tilt series[14]. Some efforts have been made to optimize these factors to achieve higher resolution with subtomogram averaging, such as 'constrained single-particle cryo-electron tomography' that uses constrained projection-matching refinement procedures[5,15,16], and dose-symmetric tilt schemes combined with exposure filtering to more efficiently use the high-resolution information from early exposure images that contain less radiation damage[17,18]. However, only averaging subtomograms of relatively thin and uncrowded samples produces nanometer (or better) resolution[5–7]. Subcellular samples are usually more crowded and thicker than these samples. It is therefore difficult to process their micrographs, and new strategies are required to push the resolution of in situ imaging to close the gap to high-resolution structure determination methods.

Here we describe TYGRESS (Fig. 1 and Supplementary Protocol), a hybrid method for resolving structures in situ in crowded cellular environments with higher resolution than was previously possible using cryo-ET and subtomogram averaging.

Results

TYGRESS, a hybrid method for in situ structural studies. TYGRESS is essentially a single-particle reconstruction from untilted high-dose (HD) images recorded with an electron dose typical for SP-cryo-EM (30–60 e^- Å^{-2}), which is 10–60 times higher than the electron dose used for individual low-dose (LD) images of a tilt series (Fig. 1a). The HD images therefore contain optimally preserved high-resolution signal by using single exposures of untilted specimens. The SP-cryo-EM reconstruction of protein assemblies

[1]Departments of Cell Biology and Biophysics, University of Texas Southwestern Medical Center, Dallas, TX, USA. [2]Janelia Farm Research Campus, Howard Hughes Medical Institute, Ashburn, VA, USA. [3]Present address: Cryo-EM Core Facility, University of Massachusetts Medical School, Worcester, MA, USA. [4]Present address: Biological Science Imaging Resource, Florida State University, Tallahassee, FL, USA. [5]These authors contributed equally: Kangkang Song, Zhiguo Shang. *e-mail: daniela.nicastro@utsouthwestern.edu

in their complex cellular context is made possible by providing additional 3D information for particle picking and initial particle alignment from the cryo-ET reconstruction, as well as subsequent subtomogram averaging that is performed on the same specimen area where an HD image is recorded (Fig. 1b,c).

In brief, the TYGRESS workflow includes: (1) for each sample area, two datasets are acquired, an HD image at 0° followed by a typical cryo-ET tilt series (Fig. 1a); (2) the cryo-ET are reconstructed, followed by subtomogram averaging of the particles of interest (Fig. 1b); (3) the information of the 3D particle position in the tomogram is projected onto the 2D HD image for particle picking (Fig. 1c and Supplementary Fig. 1), and the subtomogram angles for each particle are applied for initial particle alignment (Fig. 1c); finally (4) the particles extracted from the HD images are further processed, which includes constrained single-particle-type alignment, refinement for sub-averaged particles, and CTF and *B*-factor correction to generate the final reconstruction (Fig. 1d and Supplementary Fig. 2), whereas the cryo-ET data themselves are not included in the final TYGRESS average. There are multiple advantages of TYGRESS over cryo-ET and subtomogram averaging, including previously published strategies for cryo-ET resolution improvement, which in sum should lead to a considerable resolution improvement: (1) the higher electron dose of the HD image substantially improves the signal-to-noise ratio and thus the reliability of SP-cryo-EM refinement strategies and CTF correction; (2) HD images are recorded with an electron dose of ~30 e^- Å^{-2} (at 300 kV) and therefore are affected far less by radiation damage than images used in regular cryo-ET and subtomogram averages, which suffer accumulated doses of up to ~100 e^- Å^{-2}); and (3) the image quality of HD images is not degraded by sample tilting and multiple exposures.

Validation of TYGRESS using the ciliary axoneme. For validation, we applied TYGRESS to the intact ciliary axoneme from the multiciliated protist *Tetrahymena thermophila*, a complex cell organelle that has been extensively studied by cryo-ET and subtomogram averaging. The axoneme is the evolutionarily conserved microtubule core of cilia and flagella, with a canonical array of nine outer doublet microtubules (DMTs) surrounding two central single microtubules that form the scaffold for more than 400 different associated proteins[19] (Supplementary Fig. 3). Each DMT is composed of 96-nm repeat units, which can be treated as particles for subtomogram averaging. In the currently published cryo-ET studies of the >200-nm-thick ciliary axonemes, the achieved resolution ranged from ~3–4 nm (Fourier shell correlation (FSC) 0.5 criterion)[9,20–24], with the best resolution of 2.5 nm (FSC 0.5 criterion) being achieved using a Volta phase plate and K2 data[11]. These studies provided insights into the functional organization of axonemes, the mechanisms of dyneins and cilia motility, and ciliary dysfunction in human diseases[9,20,22]. However, the resolution of cryo-ET is still insufficient to characterize protein–protein interactions and the conformational changes that underlie cellular processes with molecular detail.

We applied TYGRESS to intact *Tetrahymena* axonemes by acquiring 99 HD images of 152 axonemes, each followed by a typical cryo-ET tilt series, and picking 18,857 particles for averaging. After constrained alignment of the picked particles from the HD images, we obtained an averaged 3D structure of the 96-nm axonemal repeat in situ with a resolution of up to 12 Å (FSC 0.143 criterion), a considerable improvement over the best previously published resolution (Figs. 2–4, Supplementary Figs. 4–6 and Supplementary Video 1). Many previously unseen molecular complexes and in situ structural details were revealed, including the 96-nm axonemal ruler and other ruler-like structures (Fig. 3a–e and Supplementary Fig. 4), individual nexin–dynein regulatory complex (N-DRC) components (Fig. 3f and Supplementary Fig. 4) and microtubule inner proteins (MIPs) (Fig. 4 and Supplementary Figs. 5 and 6). These data will shed light on the molecular mechanisms of ciliary assembly and the roles played by individual axonemal proteins in normal ciliary function.

TYGRESS reconstruction resolution improvement. The use of direct electron detectors (for example, a K2 camera) is a key reason for the recent success and resolution improvement of SP-cryo-EM[8]. However, using cryo-ET in combination with a K2 camera for subtomogram averaging of the 96-nm repeat in intact ciliary axonemes resulted only in a small resolution improvement (27.5 Å, FSC 0.5 criterion) over the cryo-ET average using a CCD camera (30 Å)[20] (Fig. 2a–d). In contrast, using TYGRESS in combination with a K2 camera, we reconstructed the 96-nm repeat up to a resolution of 12 Å (FSC 0.143 criterion, measured at the DMT regions of the axoneme) (Fig. 2a–d). Only SP-cryo-EM reconstructions of isolated and dialyzed DMTs have achieved a better resolution[25], with the caveat that all external and some internal DMT structures were lost during the DMT isolation procedure. The resolution of the TYGRESS reconstruction allows individual tubulin monomers of the DMT walls can be distinguished (Fig. 2b), facilitating generation of a pseudo-atomic model by fitting the tubulin dimer model derived from the high-resolution SP-cryo-EM map of tubulin (EMD-6353)[26] into the DMT structure. By subtracting the pseudo-atomic DMT model from the actual DMT density we calculated a structural difference map that revealed the densities of a large amount of accessory proteins and complexes (at least 20 MIPs and two previously unreported MAPs) that are assembled on the DMT scaffold (Fig. 2e).

The DMT is a highly repetitive structure, and increasing the number of averaged particles to 112,386 by averaging the 16-nm repeating units of the DMT wall and several MIP structures, allowed us to further improve the resolution from 12 Å to 10.6 Å (Fig. 2d). At this resolution, the pseudo-atomic models of individual ciliary proteins and/or domains could be reliably fitted into the structure (Fig. 2f,g).

Molecular rulers and ruler-like structures facilitate MAP docking. Our resolution-improved structure of the intact axoneme enabled the detailed visualization of known and previously uncharacterized MAP structures. Several of these MAPs are filamentous and appear to be adaptors for binding of other accessory structures to the outer surface of DMTs (Fig. 3a–e and Supplementary Fig. 4a). A previous study identified the FAP59/172 complex as a 96-nm axonemal ruler (AR) that is required for proper attachment of radial spokes (RS) RS1 and RS2, as well as inner dynein arms (IDAs) to the DMT[23]. The ruler components FAP59 and FAP172 were crudely localized using genetics and cryo-ET of cloneable tags, but the FAP59/172 complex itself could not be visualized[23]. In the TYGRESS average, the filamentous structure of the FAP59/172 complex was clearly observed running along the DMTs in the outer cleft between protofilaments A2 and A3, with two globular domains near the bases of RS1 and RS2 (AR in Fig. 3a–d and Supplementary Fig. 4a). Several axonemal complexes essential for ciliary motility seem to directly connect to the FAP59/172 filament, including RSs 1–3, N-DRC, I1 tether/tether head and some of the inner dyneins (Fig. 3d and Supplementary Video 2). By contrast, inner dyneins a and c are attached to the front-prong of RS1 and RS2, respectively. This is consistent with a previous study that demonstrated that the FAP59/172 complex is critical for docking of these structures[23].

We resolved a second long filamentous structure, here termed IDA ruler-like structure (IA-R), running along the outer surface of the DMT in the cleft between protofilaments A4 and A5 (Fig. 3b,c and Supplementary Fig. 4a). Its proximal terminus starts at a density connected with I1 between RS1 and RS2, and connects to the tail of IDA a, d and g (Fig. 3e). The direct connections between IA-R and

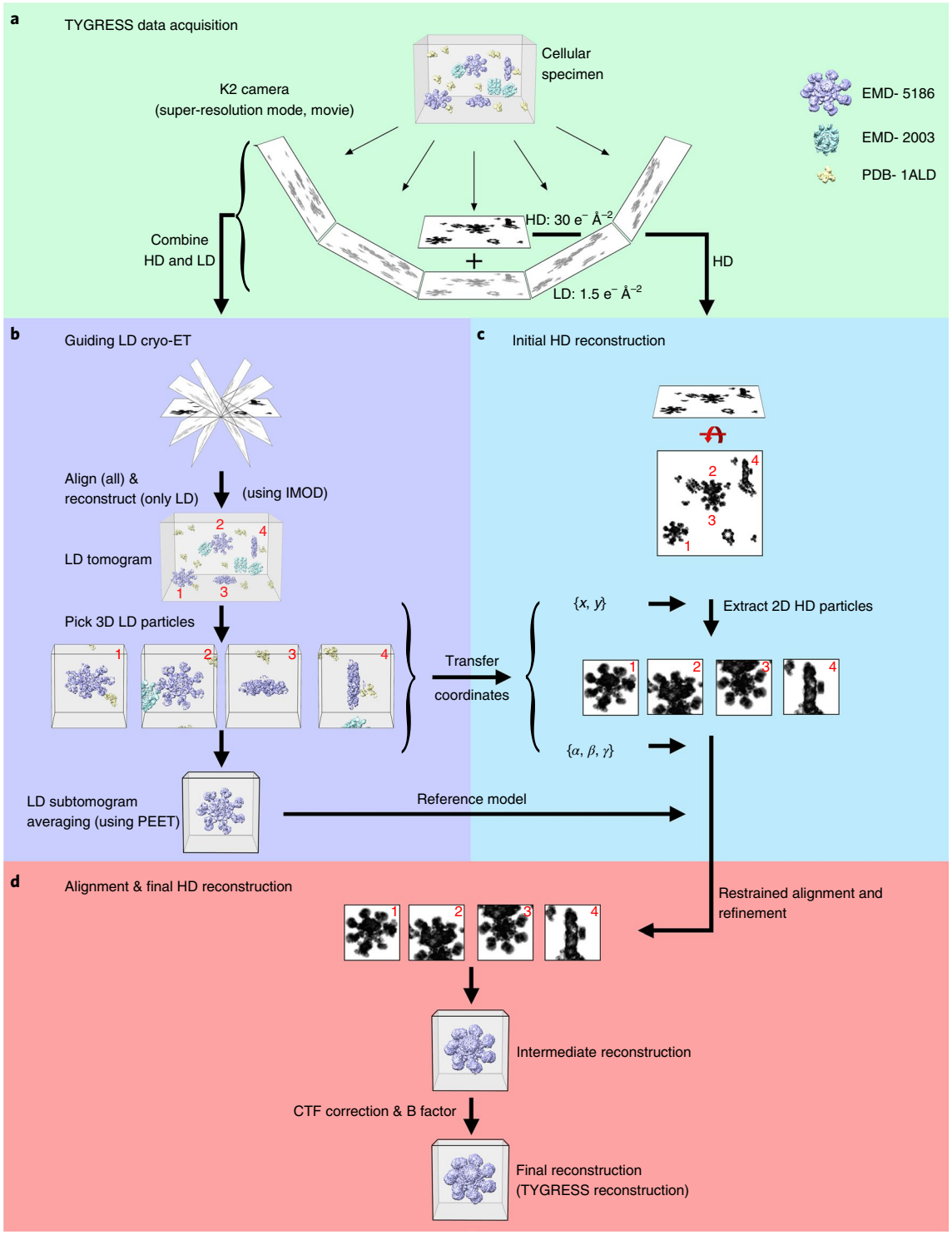

Fig. 1 | Overview of the TYGRESS workflow. To simulate a 'cellular specimen', cryo-EM structures of the apoptosome (EMD-5186, purple), GroEL (EMD-2003, cyan) and aldolase (EMD-1ALD, yellow), were randomly placed in a 3D volume. **a**, A conventional single-particle image (HD image, ~30 e^{-} Å^{-2}) is recorded, followed by a tomographic tilt series (~1.5 e^{-} Å^{-2} per LD image) of the same sample. **b**, Both the LD images and the HD image are aligned. After alignment, only the LD images are used to reconstruct a tomogram, and particles of interest are picked and subjected to subtomogram averaging. **c**, Particles of interest are picked in the HD image using the coordinates $\{x, y\}$ and orientation $\{\alpha, \beta, \gamma\}$ derived from the tomogram in **b**. **d**, The particles picked from the HD image are aligned using their corresponding orientations and locations of the subtomograms. A CTF-corrected single-particle reconstruction is calculated from the particles in the HD image and used to further refine particle orientations and locations. Finally, a negative *B* factor is applied to visualize high-resolution details.

protofilament A4 with 4-nm periodicity are clearly resolved (Fig. 3e). This periodic connection between IA-R and protofilament A4 is not observed in the region of the I1 dynein complex (Fig. 3e). Therefore, the IA-R may play a similar role to the 96-nm AR by determining the periodic docking of several IDAs. To date, the molecular composition of the IA-R has not been determined.

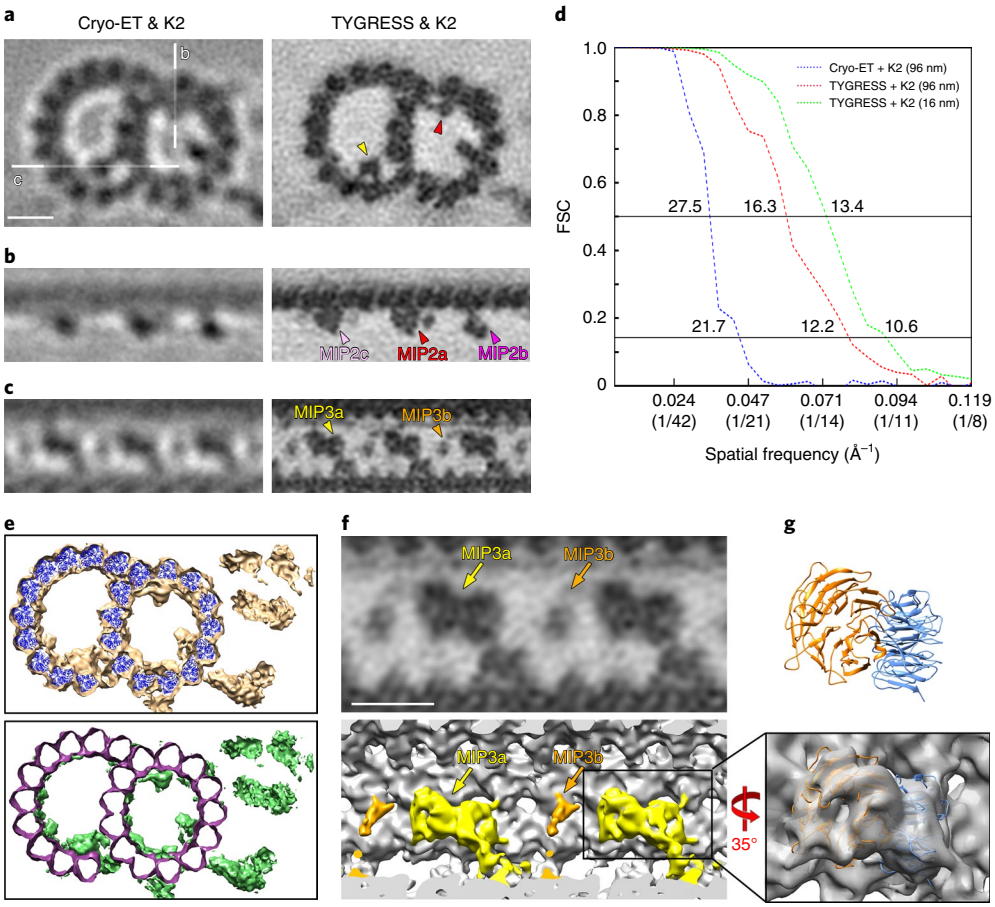

Fig. 2 | Comparison of doublet microtubules and MIPs visualized using different methods. a–c, Comparisons of electron microscopy slices of the *Tetrahymena* axonemal DMT obtained using cryo-ET (left column) and TYGRESS (right column), both using data collected on a K2 camera. Cross-sectional (**a**; viewed from proximal) and longitudinal (**b**,**c**; proximal left) electron-microscopy slices are shown. White lines in **a** (left) indicate the locations of the longitudinal slices (**b**,**c**). Scale bar, 10 nm. **d**, Resolution estimates using the FSC[49] of two independent halves of the dataset are shown for the cryo-ET and subtomogram average of the 96-nm repeat (blue; particle number 19,830) and two TYGRESS averages, that is, for the 96-nm repeat (red; particle number 18,857) and the 16-nm microtubule repeat (green; particle number 112,386). Subaveraging the 16-nm repeat further improved the final resolution from 12.2 Å to 10.6 Å at the 0.143 FSC criterion[50]. **e**, A difference map (bottom, green) was calculated between the *Tetrahymena* DMT structure obtained with TYGRESS (top, beige) and a docked pseudo-atomic model with tubulin dimers (top, blue). The remaining density (bottom, green) represents MAPs and MIPs attached to the microtubule walls. **f**, Electron-microscopy slice (top) and 3D isosurface rendering (bottom) of MIP3a (yellow) and MIP3b (orange) after averaging the 16-nm repeats. Scale bar, 10 nm. **g**, A predicted pseudo-atomic model of FAP52 (top) with two β-propellers was docked to our MIP3a density using the Chimera software package (bottom).

The outer dynein arms (ODAs) attach to the outer surface of DMTs with 24-nm periodicity, but the molecular mechanism underlying this regular docking remains unclear. The ODA docking complex (ODA-DC) has been proposed to be responsible for the 24-nm periodicity of ODAs[27]. However, purified *Chlamydomonas* ODAs can assemble with proper periodicity onto DMTs that were isolated from *oda3* mutants lacking the ODA-DC[28] suggesting that the ODA-DC does not determine ODA periodicity. The TYGRESS average reveals a 24-nm-long filamentous structure, here tentatively termed ODA ruler-like structure (OA-R) that runs along the outside cleft between protofilaments A7 and A8 (Fig. 3a,c and Supplementary Fig. 4a) and has a globular density at the docking site of the ODAs (Fig. 3d).

N-DRC base plate and linker base organization. The N-DRC is connected to neighboring DMTs[9,29,30], which is critical for restricting and thus transforming interdoublet sliding into ciliary bending motion[29,31]. The N-DRC is separated into two major regions, the base plate that is required for the N-DRC binding to the DMT and the linker region that connects to the neighboring DMT (Fig. 3f), which is critical for both axoneme integrity and ciliary motility[32]. In contrast to previous cryo-ET studies that observed the N-DRC base plate as a single rod-shaped density[33], in the TYGRESS reconstruction three N-DRC subunits were well resolved as three long filamentous structures that are twisted around each other (Fig. 3f). Twisted filaments is a common feature of cellular filaments with considerable stability and tensile strength, such as F actin and intermediate filaments[34,35]. We proposed that these filamentous structures are DRC1, DRC2 and DRC4, subunits that have previously been localized to the N-DRC base plate[29], and that are predicted to be enriched in coiled-coil domains[36].

Our structure revealed two similar N-DRC filaments (Fig. 3f) that reach from the inner junction between the A- and B-tubules, to the proximal lobe of the N-DRC, and directly connect to the 96-nm AR and the DMT. This suggests a role for these subunits in the assembly and docking of the N-DRC. We propose that these filaments are DRC1 and DRC2, because it has been shown that their absence in *pf3* and *ida6* mutant axonemes causes the loss of the entire base plate[29,36–38]. By contrast, the shorter filament with

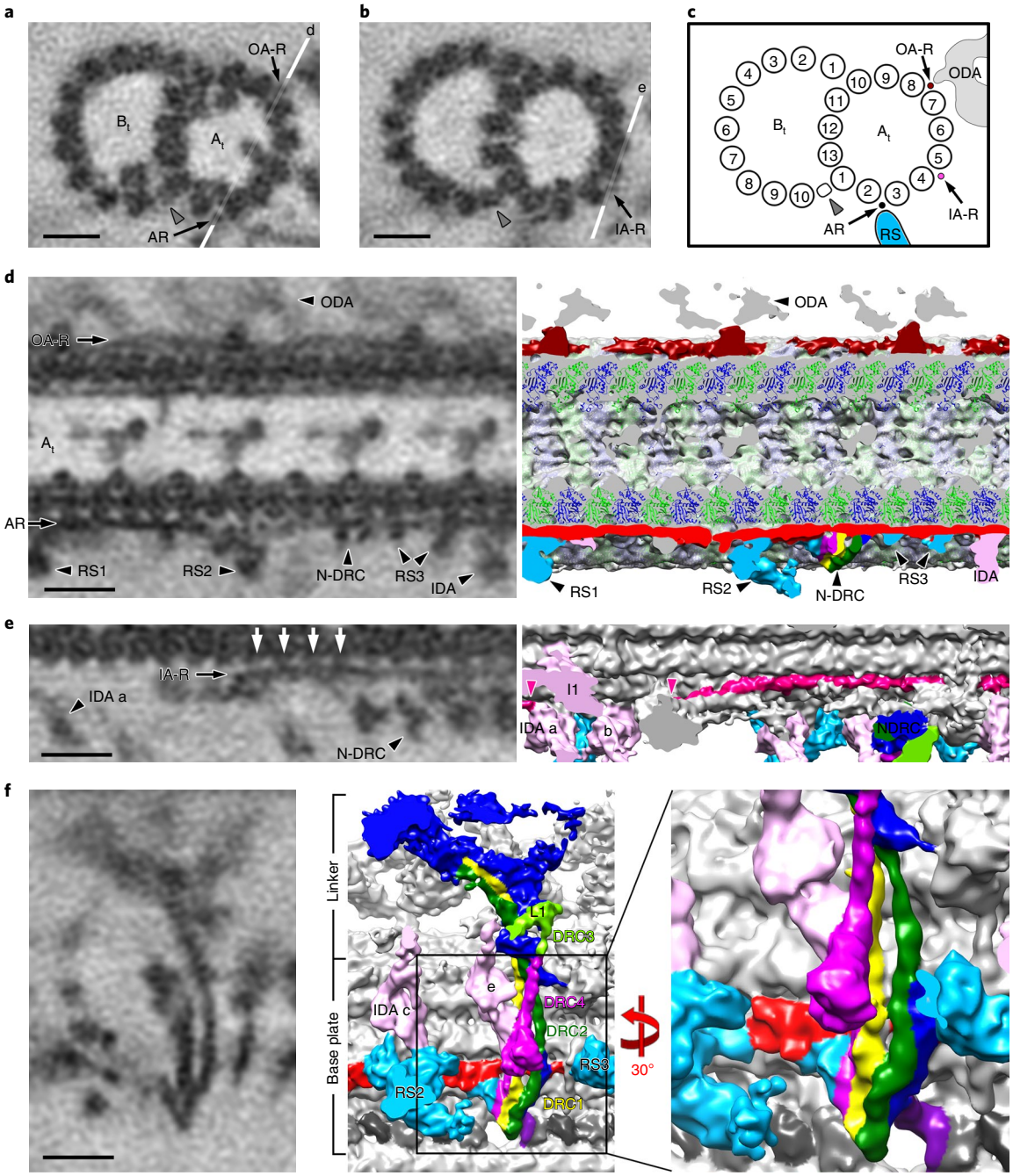

Fig. 3 | Filamentous structures and subunit architecture of the N-DRC visualized by TYGRESS. a,**b**, Cross-sectional electron-microscopy slices of averaged 96-nm axonemal repeats in two different positions showing three well-resolved filamentous structures: the 24-nm OA-R, the AR and the IA-R. White lines indicate the locations of the electron-microscopy slices shown in **d** and **e**, the gray arrowhead indicates an IJ. **c**, Schematic diagram showing the locations of the OA-R, AR, IA-R and IJ (gray arrowhead). A_t and B_t, A- and B-tubules. **d**, Longitudinal electron-microscopy slice (left) and 3D isosurface rendering (right) of the 96-nm axonemal repeat showing the OA-R (dark red) and AR (red). A tubulin dimer model is fitted into the microtubule density (positions of α- and β-tubulin on the DMT according to ref. [43]). The three RSs 1–3 (light blue), N-DRC components (purple, yellow and dark green) and IDAs (rose) are assembled onto the DMT through the AR. **e**, Longitudinal electron-microscopy slice (left) and 3D isosurface rendering (right) of the 96-nm axonemal repeat showing the IA-R (magenta). The IA-R starts between the RS1 and RS2 (right, magenta arrowhead) and attaches to and stretches along the microtubule, connecting to the tail of IDA a (left, magenta arrowhead). **f**, Electron-microscopy slice (left) and 3D isosurface rendering (middle, and expanded right) of the N-DRC structure. The coiled-coil strands of the filamentous DRC1, DRC2 and DRC4 are well resolved, comprising the base plate of the N-DRC, which contacts the 96-nm ruler (red) and the DMT and expands to the linker domain of the N-DRC. DRC1, yellow; DRC2, dark green; DRC3, light green; DRC4, purple; IDA, pink; bases of RS2 and RS3, light blue. Unknown N-DRC components are shown in dark blue. Scale bars, 10 nm.

associated globular domain (purple in Fig. 3f) binds on top of DRC1 and DRC2, and thus is likely not essential for base plate assembly, but seems to directly connect to the linker arm L1 (light green in Fig. 3f). These structural features and previously described mutant phenotypes are consistent with the short base plate filament being DRC4, which connects to DRC3 in the L1 arm[33].

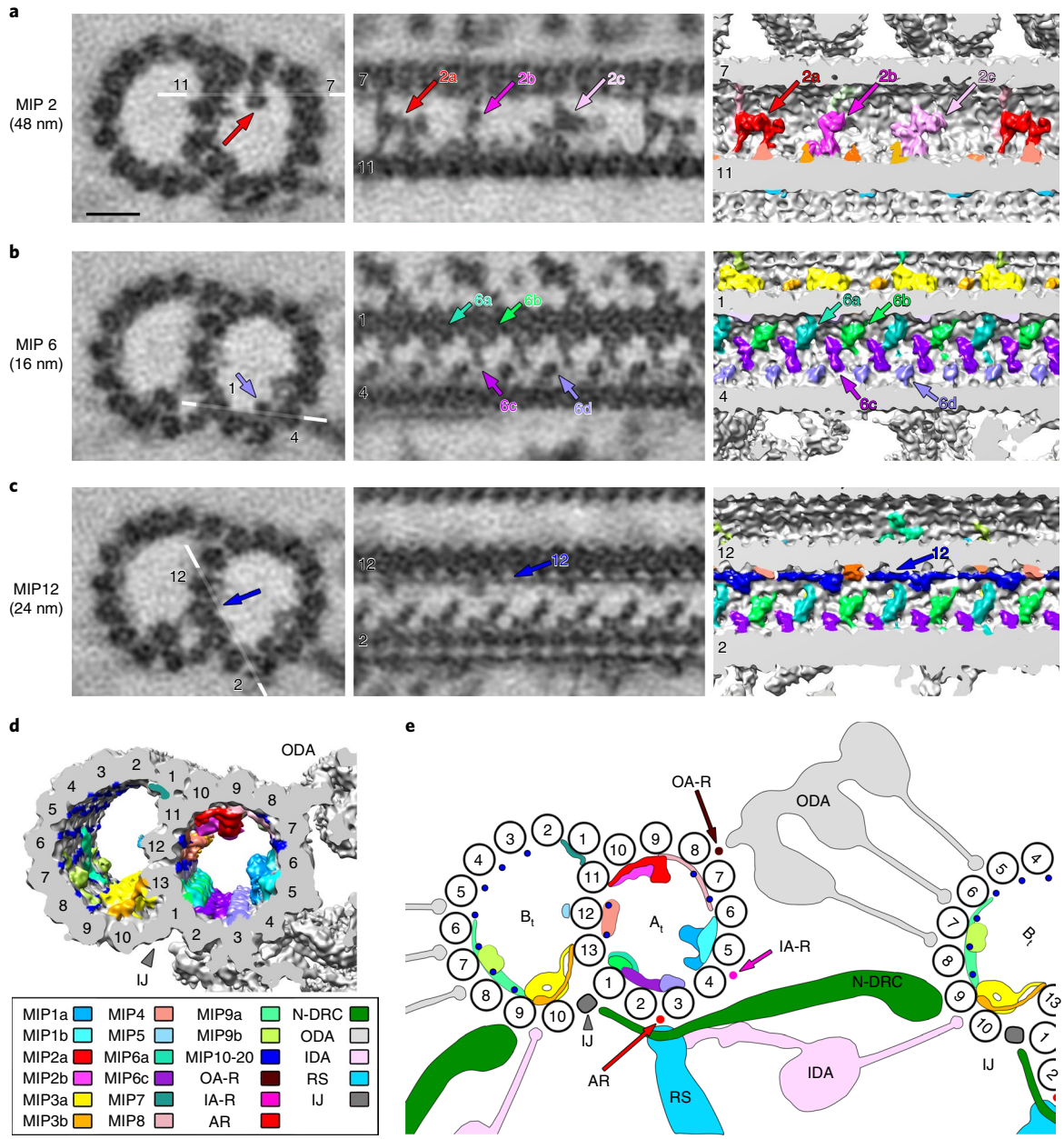

Fig. 4 | MIP structures in the intact *Tetrahymena* axonemes resolved by TYGRESS. a–c, Cross-sectional (left) and longitudinal (middle) electron-microscopy slices and longitudinal 3D isosurface renderings (right) of the averaged DMT show the structural details and diversity of selected MIP complexes (color coded as in **d**). White lines in the cross-sections indicate the locations of the respective longitudinal electron-microscopy slices. Selected protofilament numbers are indicated. MIP periodicities are indicated by the numbers inside the brackets on the left. Scale bar, 10 nm. **d**, The 3D isosurface rendering of the 96-nm axonemal repeat shows the locations of 20 MIP structures in the cross-sectional view. MIPs are colored and numbered according to their locations; the gray arrowhead indicates an IJ. **e**, Schematic summary showing the locations and interactions of axonemal complexes and protofilaments (numbered).

Inner junction organization. The inner junction (IJ) between the A- and B-tubules (also called the "B-11th density"[39]), was previously shown to be a non-tubulin connection between protofilaments A1 and B10 (ref. [40]). A recent cryo-ET study of IJ mutants showed that the IJ is composed of two proteins, FAP20 (22 kDa) and PACRG (34 kDa), which alternate along the DMT length[41]. In the latter study, hardware advances (for example, contrast increase by phase plate imaging) allowed us to improve the resolution of axonemal averages from ~3 nm to ~2.5 nm. However, even at a resolution of ~2.5 nm the densities of the two IJ proteins appeared globular and structurally indistinguishable. By contrast, in the higher resolution TYGRESS reconstruction we can clearly distinguish structural features that suggest two periodicities (Supplementary Fig. 4b–g): FAP20 (round density with a small neck; Supplementary Fig. 4c,d) and PACRG (oval-shaped density with a long filamentous extension; Supplementary Fig. 4c,d) alternate and have an 8-nm periodicity, whereas the connections between the IJ proteins and protofilament A13 have a 16-nm periodicity (Supplementary Fig. 4c,d). Our data revealed an additional density extending from the N-DRC base plate (Supplementary Fig. 4f) to one of the FAP20 subunits next to the previously reported hole on the IJ (Supplementary Fig. 4c,f), suggesting that one PACRG subunit is missing from each 96-nm repeat owing to interference with the C-terminal domains of DRC1 and DRC2.

Many MIPs bind to the inside of the A- and B-tubule walls. MIPs were discovered as structures that bind periodically to the inner surface of the ciliary DMT walls[9]. Although MIPs are proposed to increase the stability of DMTs, functional studies have not been possible because MIP proteins have not yet been identified. A recent SP-cryo-EM study of isolated DMTs has visualized the ciliary MIPs[25] but suffered from two limitations: (1) the DMTs adopt a preferred orientation in the thin ice layer on the EM grids, which has previously been observed[42] and resulted in anisotropic resolution (similar to a missing wedge in cryo-ET); and (2) the DMT isolation procedure involved high-salt extraction and dialysis to remove MAPs from the outside surface of the DMT, which also resulted in the dissociation of other structures, such as the IJ proteins[25].

In the TYGRESS reconstruction, the MIPs were well resolved and could be grouped into 20 discrete densities (MIPs 1–20) (Fig. 4 and Supplementary Figs. 5 and 6). MIPs 1–6, which have been previously observed[9,43,44], were revealed in greater structural detail, distinguishing MIP substructures. For example, the three substructures of MIP2 (MIP2a, MIP2b and MIP2c) previously appeared as three similar globular densities by cryo-ET (Fig. 2b). By contrast, the TYGRESS average clearly resolves structural differences between MIP2a, MIP2b and MIP2c (Figs. 2b and 4a, and Supplementary Fig. 5). Thus, the periodicity of the MIP2 proteins has to be corrected from the previously reported 16-nm periodicity to the 48-nm periodicity observed here. Similarly, MIP6, which was reported as a continuous structure spanning protofilaments A1–3, is now resolved as four discrete substructures, MIP6a–MIP6d (Fig. 4b and Supplementary Fig. 5).

MIPs 7–20 were not visualized by previous cryo-ET and subtomogram averaging studies but are now resolved by TYGRESS of intact ciliary axonemes (Fig. 4c and Supplementary Figs. 5 and 6), and by SP-cryo-EM of isolated DMTs[25]. The architecture resolved by TYGRESS suggests that the MIPs form a complex network that could increase the stability of the DMTs[44], for example, by strengthening the usually relatively weak lateral protofilament–protofilament interactions of microtubules[45]. The axoneme forms a scaffold in cilia that serves as a persistent platform for the attachment of hundreds of accessory proteins, making the stabilizing MIP network essential for maintaining DMT integrity under the considerable mechanical stress during ciliary beating. All of the here described MAPs, the IJ and some of the MIPs were completely missing from the high-resolution SP-cryo-EM structure of isolated DMTs[25], highlighting the critical need for a method like TYGRESS that can visualize cellular structures in situ at high resolution.

Discussion

In summary, our results demonstrate that TYGRESS can resolve macromolecular complexes at near-nanometer resolution while they are maintained in situ, that is, in their cellular context. We expect that attainable resolution can be further improved by using: (1) energy-filtered data recorded on more stable cryo-stages; (2) patch-based motion correction for the alignment of direct electron detector movie frames (MotionCor2)[46]; and (3) CTF correction that takes into account the variable z height of particles within the sample[47]. Furthermore, given larger datasets, single-particle classification could be used to calculate more homogeneous class averages, to retrieve ultrastructural differences that are biologically meaningful.

The TYGRESS method should generally improve the resolution of cellular 3D reconstructions that are amenable to subtomogram averaging, especially in cases where sample thickness and radiation damage are the main resolution-limiting factors. TYGRESS is ultimately a single-particle reconstruction method and thus will continue to benefit from the same future advances that improve SP-cryo-EM of isolated proteins complexes. However, similar to SP-cryo-EM, the preferred orientation of structures, for example, focal adhesion complexes[48] that are always oriented parallel to the EM grid, cannot be overcome by TYGRESS unless tilted HD images are included in the reconstruction. An added advantage of the cryo-ET and subtomogram averages is that they can be used to classify structurally heterogeneous complexes in 3D before calculating TYGRESS class averages.

A current challenge with TYGRESS is that data acquisition and image processing is time consuming. However, future developments of high-throughput tilt series acquisition, possibly in minutes using continuous camera exposure while the sample is tilted in quick increments with highly eucentric transmission electron microscopy specimen stages, and continued improvements to automate (batch) tilt series alignments and tomogram reconstructions, could considerably decrease the time needed for TYGRESS data acquisition and processing.

Online content

Any methods, additional references, Nature Research reporting summaries, source data, extended data, supplementary information, acknowledgements, peer review information, details of author contributions and competing interests, and statements of code and data availability are available at https://doi.org/10.1038/s41592-019-0651-0.

Received: 28 August 2018; Accepted: 11 October 2019;
Published online: 25 November 2019

References

1. Bai, X. C., McMullan, G. & Scheres, S. H. How cryo-EM is revolutionizing structural biology. *Trends Biochem. Sci.* **40**, 49–57 (2015).
2. Cheng, Y. Single-particle cryo-EM at crystallographic resolution. *Cell* **161**, 450–457 (2015).
3. Herzik, M. A. Jr., Wu, M. & Lander, G. C. Achieving better-than-3-Å resolution by single-particle cryo-EM at 200 keV. *Nat. Methods* **14**, 1075–1078 (2017).
4. Bartesaghi, A. et al. Atomic resolution cryo-EM structure of β-galactosidase. *Structure* **26**, 848–856 (2018).
5. Bartesaghi, A., Lecumberry, F., Sapiro, G. & Subramaniam, S. Protein secondary structure determination by constrained single-particle cryo-electron tomography. *Structure* **20**, 2003–2013 (2012).
6. Schur, F. K. et al. An atomic model of HIV-1 capsid-SP1 reveals structures regulating assembly and maturation. *Science* **353**, 506–508 (2016).
7. Wan, W. et al. Structure and assembly of the ebola virus nucleocapsid. *Nature* **551**, 394–397 (2017).
8. Cheng, Y., Grigorieff, N., Penczek, P. A. & Walz, T. A primer to single-particle cryo-electron microscopy. *Cell* **161**, 438–449 (2015).
9. Nicastro, D. et al. The molecular architecture of axonemes revealed by cryoelectron tomography. *Science* **313**, 944–948 (2006).
10. Briggs, J. A. Structural biology in situ—the potential of subtomogram averaging. *Curr. Opin. Struct. Biol.* **23**, 261–267 (2013).
11. Fu, G. et al. The I1 dynein-associated tether and tether head complex is a conserved regulator of ciliary motility. *Mol. Biol. Cell* **29**, 1048–1059 (2018).
12. Briegel, A. et al. New insights into bacterial chemoreceptor array structure and assembly from electron cryotomography. *Biochemistry* **53**, 1575–1585 (2014).
13. Crowther, R. A., Derosier, D. J. & Klug, A. The reconstruction of a three-dimensional structure from projections and its application to electron microscopy. *Proc. R. Soc. Lond. Ser. A* **317**, 319–340 (1970).
14. Brilot, A. F. et al. Beam-induced motion of vitrified specimen on holey carbon film. *J. Struct. Biol.* **177**, 630–637 (2012).
15. Himes, B. A. & Zhang, P. emClarity: software for high-resolution cryo-electron tomography and subtomogram averaging. *Nat. Methods* **15**, 955–961 (2018).
16. Yu, L., Snapp, R. R., Ruiz, T. & Radermacher, M. Projection-based volume alignment. *J. Struct. Biol.* **182**, 93–105 (2013).
17. Grant, T. & Grigorieff, N. Measuring the optimal exposure for single particle cryo-EM using a 2.6 Å reconstruction of rotavirus VP6. *eLife* **4**, e06980 (2015).
18. Hagen, W. J. H., Wan, W. & Briggs, J. A. G. Implementation of a cryo-electron tomography tilt-scheme optimized for high resolution subtomogram averaging. *J. Struct. Biol.* **197**, 191–198 (2017).
19. Pazour, G. J., Agrin, N., Leszyk, J. & Witman, G. B. Proteomic analysis of a eukaryotic cilium. *J. Cell Biol.* **170**, 103–113 (2005).
20. Lin, J. & Nicastro, D. Asymmetric distribution and spatial switching of dynein activity generates ciliary motility. *Science* **360**, eaar1968 (2018).

21. Lin, J., Okada, K., Raytchev, M., Smith, M. C. & Nicastro, D. Structural mechanism of the dynein power stroke. *Nat. Cell Biol.* **16**, 479–485 (2014).
22. Lin, J. et al. Cryo-electron tomography reveals ciliary defects underlying human RSPH1 primary ciliary dyskinesia. *Nat. Commun.* **5**, 5727 (2014).
23. Oda, T., Yanagisawa, H., Kamiya, R. & Kikkawa, M. A molecular ruler determines the repeat length in eukaryotic cilia and flagella. *Science* **346**, 857–860 (2014).
24. Pigino, G. et al. Cryoelectron tomography of radial spokes in cilia and flagella. *J. Cell Biol.* **195**, 673–687 (2011).
25. Ichikawa, M. et al. Subnanometre-resolution structure of the doublet microtubule reveals new classes of microtubule-associated proteins. *Nat. Commun.* **8**, 15035 (2017).
26. Zhang, R., Alushin, G. M., Brown, A. & Nogales, E. Mechanistic origin of microtubule dynamic instability and its modulation by EB proteins. *Cell* **162**, 849–859 (2015).
27. Owa, M. et al. Cooperative binding of the outer arm-docking complex underlies the regular arrangement of outer arm dynein in the axoneme. *Proc. Natl Acad. Sci. USA* **111**, 9461–9466 (2014).
28. Oda, T., Abe, T., Yanagisawa, H. & Kikkawa, M. Docking-complex-independent alignment of *Chlamydomonas* outer dynein arms with 24-nm periodicity in vitro. *J. Cell Sci.* **129**, 1547–1551 (2016).
29. Heuser, T., Raytchev, M., Krell, J., Porter, M. E. & Nicastro, D. The dynein regulatory complex is the nexin link and a major regulatory node in cilia and flagella. *J. Cell Biol.* **187**, 921–933 (2009).
30. Huang, B., Ramanis, Z. & Luck, D. J. Suppressor mutations in *Chlamydomonas* reveal a regulatory mechanism for flagellar function. *Cell* **28**, 115–124 (1982).
31. Summers, K. E. & Gibbons, I. R. Adenosine triphosphate-induced sliding of tubules in trypsin-treated flagella of sea-urchin sperm. *Proc. Natl Acad. Sci. USA* **68**, 3092–3096 (1971).
32. Alford, L. M. et al. The nexin link and B-tubule glutamylation maintain the alignment of outer doublets in the ciliary axoneme. *Cytoskeleton* **73**, 331–340 (2016).
33. Song, K. et al. In situ localization of N and C termini of subunits of the flagellar nexin–dynein regulatory complex (N-DRC) using SNAP tag and cryo-electron tomography. *J. Biol. Chem.* **290**, 5341–5353 (2015).
34. von der Ecken, J. et al. Structure of the F-actin–tropomyosin complex. *Nature* **519**, 114–117 (2015).
35. Herrmann, H. & Aebi, U. Intermediate filaments: structure and assembly. *Cold Spring Harb. Perspect. Biol.* **8**, a018242 (2016).
36. Lin, J. et al. Building blocks of the nexin–dynein regulatory complex in *Chlamydomonas* flagella. *J. Biol. Chem.* **286**, 29175–29191 (2011).
37. Bower, R. et al. DRC2/CCDC65 is a central hub for assembly of the nexin–dynein regulatory complex and other regulators of ciliary and flagellar motility. *Mol. Biol. Cell* **29**, 137–153 (2018).
38. Wirschell, M. et al. The nexin–dynein regulatory complex subunit DRC1 is essential for motile cilia function in algae and humans. *Nat. Genet.* **45**, 262–268 (2013).
39. Linck, R. et al. Insights into the structure and function of ciliary and flagellar doublet microtubules: tektins, Ca^{2+}-binding proteins, and stable protofilaments. *J. Biol. Chem.* **289**, 17427–17444 (2014).
40. Nicastro, D. et al. Cryo-electron tomography reveals conserved features of doublet microtubules in flagella. *Proc. Natl Acad. Sci. USA* **108**, E845–E853 (2011).
41. Dymek, E. E. et al. PACRG and FAP20 form the inner junction of axonemal doublet microtubules and regulate ciliary motility. *Mol. Biol. Cell* **30**, 1805–1816 (2019).
42. Sui, H. & Downing, K. H. Molecular architecture of axonemal microtubule doublets revealed by cryo-electron tomography. *Nature* **442**, 475–478 (2006).
43. Maheshwari, A. et al. α- and β-tubulin lattice of the axonemal microtubule doublet and binding proteins revealed by single particle cryo-electron microscopy and tomography. *Structure* **23**, 1584–1595 (2015).
44. Owa, M. et al. Inner lumen proteins stabilize doublet microtubules in cilia and flagella. *Nat. Commun.* **10**, 1143 (2019).
45. Nogales, E., Whittaker, M., Milligan, R. A. & Downing, K. H. High-resolution model of the microtubule. *Cell* **96**, 79–88 (1999).
46. Zheng, S. Q. et al. MotionCor2: anisotropic correction of beam-induced motion for improved cryo-electron microscopy. *Nat. Methods* **14**, 331–332 (2017).
47. Turonova, B., Schur, F. K. M., Wan, W. & Briggs, J. A. G. Efficient 3D-CTF correction for cryo-electron tomography using NovaCTF improves subtomogram averaging resolution to 3.4 Å. *J. Struct. Biol.* **199**, 187–195 (2017).
48. Geiger, B., Spatz, J. P. & Bershadsky, A. D. Environmental sensing through focal adhesions. *Nat. Rev. Mol. Cell Biol.* **10**, 21–33 (2009).
49. Harauz, G. & Van Heel, M. Exact filters for general geometry three dimensional reconstruction. *Optik* **73**, 146–156 (1986).
50. Rosenthal, P. B. & Henderson, R. Optimal determination of particle orientation, absolute hand, and contrast loss in single-particle electron cryomicroscopy. *J. Mol. Biol.* **333**, 721–745 (2003).

Methods

Cryo-sample preparation. Wild-type axonemes were isolated from *Tetrahymena thermophila* strain CU428 as previously described[22]. In brief, cilia were detached from cells using the pH-shock method[51] and purified by centrifugation at 2,400*g*, 4 °C for 10 min (twice). Purified cilia were demembranated using 1% IGEPAL CA-630 (Sigma Aldrich) in HMEEK buffer (30 mM HEPES, pH 7.4, 5 mM $MgSO_4$, 1 mM EGTA, 0.1 mM EDTA and 25 mM KCl) and axonemes were collected by centrifugation at 10,000*g*, 4 °C, for 10 min. The axoneme pellet was carefully resuspended in HMEEK buffer and cryo-samples were prepared as previously described[21]. In brief, Quantifoil grids (Quantifoil MicroTools) were glow discharged for 30 s at −40 mA before use, coated with 10-nm colloidal gold (Sigma Aldrich) and loaded on a plunge-freezing device. Then, 3 µl of axoneme sample and 1 µl of a five-fold-concentrated 10-nm BSA-coated, colloidal gold solution[52] was added to the grid and mixed. The grid was blotted with filter paper for 1.5–2.5 s and immediately frozen by plunging into liquid ethane. The vitrified samples were then stored in liquid nitrogen until examination by electron microscopy.

Image acquisition. The frozen grid was mounted in a cryo-holder (Gatan) and imaged on a Tecnai F30 transmission electron microscope (FEI) equipped with a field emission gun and operated at 300 keV. The data were collected under low-dose conditions using the SerialEM software[53]. For each intact axoneme, two sets of data were collected using a K2 direct electron detector (Gatan) at a magnification of ×9,400. First, a movie stack (80 frames) was collected at 0° with a total electron dose of ~30 e^- $Å^{-2}$ (HD image) at varying defocuses of −1.5 µm to −3 µm in the K2 super-resolution mode; second, a typical tilt series with an accumulated electron dose of ~100 e^- $Å^{-2}$ (LD images) was recorded in the K2 counting mode at a defocus of −8 µm using a bidirectional tilt scheme, that is, a continuous series of tilt images was recorded from 0° to −64° with 2° increments, followed by a second series from 2° to 64°. At each tilt angle, a movie stack (five frames) with an exposure time of 2 s and an electron dose of 1.5 e^- $Å^{-2}$ was recorded. The resulting pixel sizes of the 0° HD image and the LD images were 0.2112 nm and 0.4224 nm, respectively. The parameters used for data collection are summarized in Supplementary Table 2.

Image processing. Full-frame motion correction of the movie stacks was performed using IMOD scripts[54]. Then, both the HD image and LD images were aligned using fiducial markers. The LD images alone were further reconstructed into a 3D tomogram by weighted back projection using the IMOD software package. Subtomograms containing the 96-nm axonemal repeats were extracted from the tomograms, aligned and averaged using PEET[9]. The HD images were used to reconstruct high-resolution structures of the 96-nm axonemal repeats with the TYGRESS method developed in this study (Supplementary Protocol). FREALIGN[55] was used for the final reconstructions as part of TYGRESS. CTFFIND3 (ref. [56]) was used to detect defocus values; the power spectra of about 200 patches with dimension of 256×256 pixels were averaged to generate the CTF. BFACTOR[57] was used to sharpen and filter the final reconstruction. The pseudo-atomic model of MIP3a/FAP52 was generated and calculated from the protein sequence using the ExPASy online tool, SWISS-MODEL[58]. UCSF Chimera[59] was used for 3D visualization and high-resolution structure fitting (for example, X-ray, pseudo-atomic model).

Resolution measurement. The resolution of the TYGRESS reconstruction was measured using the FSC[49]. In brief, the dataset was divided into two halves using even and odd indexes at the outset; initial reference models for each dataset were generated using the corresponding subtomogram averaged structure; then the two halves were aligned and reconstructed independently and the FSC between the two reconstructions was calculated.

TYGRESS image processing. TYGRESS is essentially a single-particle reconstruction method using coordinate information provided by cryo-ET to enable particle picking (Fig. 1). During imaging, two datasets were acquired for each region of interest: a 2D image (HD image) at 0° tilt for the final TYGRESS reconstruction using an electron dose typical for conventional SP-cryo-EM and a traditional LD tilt series (LD images) that was used for positional information. To minimize the effects of radiation damage in the final reconstruction, the HD image was recorded before the LD images (Fig. 1a).

Alignment of the combined tilt series and tomogram reconstruction with subtomogram averaging. During image processing, each HD image was inserted into the corresponding tilt series at the angle corresponding to where the HD image was taken (for example, an HD image recorded at 0° was inserted just before the LD image at 0°) using the command 'newstack' in IMOD, resulting in a 'combined tilt series'. The combination of HD and LD images ensured a common reference frame for the later steps in the TYGRESS procedure. The combined tilt series was then aligned on the basis of the 10-nm gold fiducial markers using the IMOD software package. However, only the LD images were used to calculate a tomogram after alignment, and then subtomogram averaging was performed using PEET (Fig. 1b). Here the 96-nm repeat unit of the axoneme can be readily identified on the basis of structural features such as the doublet microtubule (MT) walls and the RSs, which allowed us to pick particles of 240×240×240 pixels (240×0.4224 nm = 101 nm) from the noisy raw tomograms. Subtomogram averaging was performed using the raw tomogram and a reference, which was constantly updated using the average structure of the last iteration. In total, 19,830 particles were picked from 152 axoneme tomograms and aligned in PEET for subtomogram averaging.

The HD image was excluded for tomogram reconstruction and subtomogram averaging to avoid (1) reconstruction artifacts owing to uneven weighting of the HD and LD images in the tomogram and (2) alignment bias in the initial reconstruction calculated from the HD image.

Retrieval of coordinates and orientations for picking the particle in 2D on the HD image. Because the HD image was aligned together with the LD images during tomographic reconstruction, we could retrieve the 2D HD image particle coordinates and orientations that correspond to the subtomogram particles in the 3D tomogram. The final coordinates $\{x, y\}$ and orientations $\{\alpha, \beta, \gamma\}$ for each 2D HD image particle are given as:

$$N^{sp}_{(x,y)} = N^{\mathrm{IMOD}}_{(\delta x,\delta y)} + \mathrm{Proj}_{(\mathrm{xy\ plane})}\left[\mathrm{F}^{-1}_{\mathrm{IMOD(C)}}\mathrm{N}^{\mathrm{PEET}}_{(\mathrm{x,y,z})}\right] \quad (1)$$

$$N^{sp}_{(\alpha,\beta,\gamma)} = N^{\mathrm{IMOD}}_{(\delta\alpha,\delta\beta,\delta\gamma)} + F^{-1}_{\mathrm{IMOD(O)}}N^{\mathrm{PEET}}_{(\alpha,\beta,\gamma)} \quad (2)$$

Where, $(\delta x,\delta y)$ and $(\delta a, \delta\beta, \delta\gamma)$ are the HD image shift and rotation from the fiducial gold alignment of the combined tilt series; $N^{\mathrm{PEET}}_{(x,y,z)}$ and $N^{\mathrm{PEET}}_{(\alpha,\beta,\gamma)}$ are the 3D particle coordinates and orientations in the tomogram after PEET alignment; and $F^{-1}_{\mathrm{IMOD(C)}}$ and $F^{-1}_{\mathrm{IMOD(O)}}$ represent the inverse transformations for coordinates and orientations of particles in the HD image, which has the same parameters as the 0° tilt LD image of the tomogram. $\mathrm{Proj}_{(xy\ \mathrm{plane})}$ converts the 3D coordinates to 2D coordinates in the HD image.

2D particle picking from HD image. The command 'EXCISE' from the IMOD package was used to extract particles from the HD image according to the coordinates determined from the tomogram. In this work, the particle box size was set to 320×320 pixels, which corresponds to the size of the 3D volume extracted from the tomogram. This size (320×0.4224 = 135 nm) is sufficient to cover an entire 96-nm axonemal repeat. An example of how TYGRESS successfully identified the particle center from the overlapping projection images of an axoneme is shown in Supplementary Fig. 1.

Constrained alignment and reconstruction of the 2D HD particles. Before the 3D reconstruction of the particle of interest can be calculated using all particle images that were extracted from the 2D HD images, the particle images, which represent projections of the particle in different orientations, have to be aligned. A variety of algorithms and image-processing methods have been developed to facilitate 2D and 3D particle alignment[8,60], including approaches specifically developed to improve alignment in cases where structural information overlaps in the experimental 2D images. Latter methods usually preprocess the data to reduce negative effects of the background information on the accuracy of the target particle alignment, for example, by using the high-spatial-frequency information and a whitening filter to detect proteins in crowded cellular environments[61], or by 'signal subtraction' from the experimental particle images before performing (focused) alignments. The 'signal subtraction' approach has been used to reconstruct membrane proteins embedded in liposomes[62] and proteins decorating microtubules[63], and to dissect continuous structural heterogeneity in cryo-EM single-particle data using multibody refinement[64].

Here we developed an alignment-refinement algorithm that is tailored toward samples containing many copies of the particle of interest that might also overlap in the 2D HD images, such as in the cylindrically organized axonemal repeat, which is studied here, or other samples previously studied by subtomogram averaging (for example, COPI and II vesicle coats[65,66], HIV envelope glycoproteins[6,67], the tubular contractile injection systems in bacteria[68] or crowded nucleosomes in nuclei[69]). However, depending on the nature of the sample, TYGRESS can also be combined with other existing (for example, whitening filter[61]) or newly developed alignment-refinement approaches (as described below). The alignment approach developed here combines the information provided by the previous subtomogram averaging step and elements from iterative reprojection-based alignment[16]. Specifically, we generate and iteratively refine an alignment reference for each particle to be aligned that both reprojects the latest 3D particle average in the position and orientation of the target particle, and sums the reprojections of all particles that contribute to the overlapping information in the experimental 2D HD image for the target particle to best match the reference with the experimental 2D particle image. Initial position and angular orientations of the particles (α, β and γ) are provided by the subtomogram averaging step, and the parameters are then iteratively refined over several alignment rounds.

The 2D HD particle image alignment is performed as 'constrained alignment' because, in the 2D HD images, the particle information is convoluted by information from the complex environment that surrounds the particle and thus overlaps the particle information in the 2D HD projection image. Cross-correlation alignment

between the 2D HD particle image and 2D reference images that are generated by reprojecting a 3D reference using the full euler angle space could cause 'false' cross-correlation peaks with background features and thus result in misalignment of the target particle. By contrast, the alignment during the subtomogram averaging step can be performed without constraining the angular search range, because the 3D reconstructed particles in the raw tomograms are not convoluted by overlapping background information that could generate misalignment. Thus, an advantage of TYGRESS is that not only the subtomogram average itself can be used as initial reference, but also the subtomogram alignment parameters can be used as a good initial alignment that only requires small refinements driven by the high-frequency (high-resolution) information that is present in the 2D HD particle images, but is degraded in the lower-resolution subtomogram volumes owing to radiation damage. Thus for the 'constrained alignment' of the 2D HD particle images the parameter changes are limited to a user-defined range around the initial subtomogram averaging alignment; for example, in our study, the initial range for allowed alignment changes was set to ±4 nm positional and ±5° angular changes from the subtomogram averaging alignment.

Using the coordinates retrieved from the subtomogram averaging step, we calculated the position of each target particle and of 'neighboring' particles that overlap in the 2D HD image with the target particle (the radius for how many particles to include is user-defined in the TYGRESS input file). For the constrained cross-correlation alignment of each target particle picked from the 2D HD images, a set of 2D reference images was generated by performing the following steps. (1) For the target and all 'neighboring' particles that will be included, 2D reprojection images were generated from the latest 3D reference model—initially this is the subtomogram average. For the reprojection of the 'neighboring' particles the angles from the subtomogram averaging were used. For the target particle, a set of reprojections was calculated that varied by a user-defined range (1° steps) around the subtomogram averaging angles. (2) Each target-particle reprojection was then combined with the reprojections of the 'neighboring' particles using the relative positions between the included particles to generate the correlating 2D reference image. This resulted in a target-particle-specific set of 2D reference images that varied only slightly in the orientation of the target particle. In a next step, the 2D HD particle image was then cross-correlated to each 2D reference from the set, and the match with the highest cross-correlation coefficient was used to update the alignment parameters of the target particle. This was performed for each particle picked from the 2D HD images.

The constrained alignment is iterative in nature, with the first iteration refining the subtomogram averaging positional and angular parameters (*x* and *y* shifts, and angles) for each target particle. For the next iteration of the constrained alignment, the refined alignment parameters for each particle are used to generate updated reference models for each target particle and the search constraints are tightened, that is, for instance, to 1 nm shift and 2° angular deviation from the parameters obtained in the previous round. After several iterations, a final set of parameters for each target particle is generated and used for the 3D reconstruction of the particle of interest.

CTF estimation of the HD images, as well as the first round of constrained alignment, was performed using movie averages that contained all frames (for example, frames 1–80 in this work) (Supplementary Fig. 2). To account for local beam-induced sample motion that was not corrected by the whole-frame alignment in IMOD, subframe averages were calculated using frames 3–21, 22–40, 41–59 and 60–78 (the initial two frames were excluded owing to in-frame blurring), and the following rounds of constrained alignment was done using each of these subframes. The aligned particles from these subframes were then recombined to calculate the 3D reconstruction (Fig. 1). The latter step could potentially be avoided if motion correction is performed on image patches rather than global whole-frame alignments. Moreover, to improve the alignment of substructures (such as dynein arms within the large 96-nm axonemal repeat), we occasionally focused the alignment on these by masking neighboring densities.

The alignment method we describe here for the 2D HD particle images, using composed 2D reprojected references, is well suited for samples in which the tomographic volumes contain many particle copies, as their densities can be summed to generate references that account for parts of the overlapping densities in the experimental 2D HD images. Therefore, samples that would benefit most from this algorithm include, for example, cytoskeletal assemblies with multiple repeats (for example, muscle sarcomeres and actin networks), viruses and vesicle-bound proteins. However, users can also combine other existing or newly developed alignment methods with TYGRESS. For example, in cytosolic environments with non-averageable background information surrounding the particles of interest, alignment methods that involve subtracting background or applying a whitening filter to the experimental 2D HD images may be advantageous[61,62,64]. To combine alternate alignment methods with TYGRESS, users should skip step 5.5 in the step-by-step protocol (step 3 in the TYGRESS graphical user interface (GUI)) and instead use the initial alignment parameters from the subtomogram averaging that are provided as output from step 5.4 (step 2 in the TYGRESS GUI) in the .par file. After performing alignment refinement externally, the users can add the refined alignment parameters into the .par file and replace the old .par file before continuing with step 5.6 (step 4 in the TYGRESS GUI) to calculate the final reconstruction (the file format for .par is provided as template in folder '/example/combined_PEET/HD_particles/WT_20120914_S1/' after TYGRESS installation).

Similar to subtomogram averages of cellular samples, the quality and resolution of TYGRESS reconstructions of subcellular structures could ultimately be limited by the background added by overlapping unrelated structures within crowded environments. Although randomly distributed unrelated structures will be averaged out, resulting in a smooth background, the absolute contrast between the averaged particle and the background is smaller as compared to the contrast achievable in SP-cryo-EM between the isolated proteins and the surrounding aqueous buffer.

Statistics and reproducibility. All samples used in this work were from two independent sample preparations. In total, 99 HD images, each followed by a typical cryo-ET tilt series (with 1–2 axonemes per series) were collected during 11 cryo-EM data acquisition sessions, resulting in tomographic reconstructions of 152 axonemes. A total of 19,830 particles were picked for cryo-ET and subtomogram averaging of the 96-nm axonemal repeat. A total of 18,857 (112,386) particles picked from HD images were used to generate the TYGRESS average of the 96-nm axonemal (16-nm microtubule) repeat.

Reporting Summary. Further information on research design is available in the Nature Research Reporting Summary linked to this article.

Data availability

The TYGRESS reconstructions have been deposited in the Electron Microscopy Data Bank under accession code EMD-9023. All other data that support the findings of this study are available in the manuscript or its Supplementary Information. Raw image data (that is, HD images and corresponding tilt series) used to generate the TYGRESS average and figures in this study are available from the corresponding author upon request.

Code availability

TYGRESS source code and documentation are available on Code Ocean (https://doi.org/10.24433/CO.2034333.v1). The TYGRESS program is also available at https://www.utsouthwestern.edu/labs/nicastro/tygress/. A user manual is available as a Supplementary Protocol (https://doi.org/10.21203/rs.2.16083/v1).

References

51. Witman, G. B., Carlson, K., Berliner, J. & Rosenbaum, J. L. *Chlamydomonas* flagella. I. Isolation and electrophoretic analysis of microtubules, matrix, membranes, and mastigonemes. *J. Cell Biol.* **54**, 507–539 (1972).
52. Iancu, C. V. et al. Electron cryotomography sample preparation using the vitrobot. *Nat. Protoc.* **1**, 2813–2819 (2006).
53. Mastronarde, D. N. Automated electron microscope tomography using robust prediction of specimen movements. *J. Struct. Biol.* **152**, 36–51 (2005).
54. Kremer, J. R., Mastronarde, D. N. & McIntosh, J. R. Computer visualization of three-dimensional image data using IMOD. *J. Struct. Biol.* **116**, 71–76 (1996).
55. Grigorieff, N. FREALIGN: high-resolution refinement of single particle structures. *J. Struct. Biol.* **157**, 117–125 (2007).
56. Mindell, J. A. & Grigorieff, N. Accurate determination of local defocus and specimen tilt in electron microscopy. *J. Struct. Biol.* **142**, 334–347 (2003).
57. Fernandez, J. J., Luque, D., Caston, J. R. & Carrascosa, J. L. Sharpening high resolution information in single particle electron cryomicroscopy. *J. Struct. Biol.* **164**, 170–175 (2008).
58. Biasini, M. et al. SWISS-MODEL: modelling protein tertiary and quaternary structure using evolutionary information. *Nucleic Acids Res.* **42**, W252–W258 (2014).
59. Pettersen, E. F. et al. UCSF Chimera—a visualization system for exploratory research and analysis. *J. Comput. Chem.* **25**, 1605–1612 (2004).
60. Sigworth, F. J. Principles of cryo-EM single-particle image processing. *Microscopy* **65**, 57–67 (2016).
61. Rickgauer, J. P., Grigorieff, N. & Denk, W. Single-protein detection in crowded molecular environments in cryo-EM images. *eLife* **6**, e25648 (2017).
62. Jensen, K. H., Brandt, S. S., Shigematsu, H. & Sigworth, F. J. Statistical modeling and removal of lipid membrane projections for cryo-EM structure determination of reconstituted membrane proteins. *J. Struct. Biol.* **194**, 49–60 (2016).
63. Narita, A., Mizuno, N., Kikkawa, M. & Maeda, Y. Molecular determination by electron microscopy of the dynein–microtubule complex structure. *J. Mol. Biol.* **372**, 1320–1336 (2007).
64. Nakane, T., Kimanius, D., Lindahl, E. & Scheres, S. H. Characterisation of molecular motions in cryo-EM single-particle data by multi-body refinement in RELION. *eLife* **7**, e36861 (2018).
65. Bykov, Y. S. et al. The structure of the COPI coat determined within the cell. *eLife* **6**, e32493 (2017).

66. Zanetti, G. et al. The structure of the COPII transport-vesicle coat assembled on membranes. *eLife* **2**, e00951 (2013).
67. Bartesaghi, A., Merk, A., Borgnia, M. J., Milne, J. L. & Subramaniam, S. Prefusion structure of trimeric HIV-1 envelope glycoprotein determined by cryo-electron microscopy. *Nat. Struct. Mol. Biol.* **20**, 1352–1357 (2013).
68. Bock, D. et al. In situ architecture, function, and evolution of a contractile injection system. *Science* **357**, 713–717 (2017).
69. Cai, S., Bock, D., Pilhofer, M. & Gan, L. The in situ structures of mono-, di-, and trinucleosomes in human heterochromatin. *Mol. Biol. Cell* **29**, 2450–2457 (2018).

Acknowledgements

We thank C. Xu for training and for maintaining the electron microscopy facility at Brandeis University; J. Heumann and D. Mastronarde for technical advice concerning cryo-ET and subtomogram averaging; A. Rohou and S. C. Harrison for helpful discussions; T. Ni, J. Pinskey and G. Riddihough for critically reading the manuscript; and R. Zhang for providing the EM structure of the tubulin dimer for docking. This work was supported by funding from the National Institutes of Health (grant R01 GM111506 to D.N.) and the Cancer Prevention and Research Institute of Texas (grant RR140082 to D.N.). N.G. is an investigator of the Howard Hughes Medical Institute.

Author contributions

D.N. conceived the study and designed experiments; Z.S. and X.F. programmed; K.S. collected and processed the data with Z.S; N.G. contributed scientific and technical insights throughout the project; and Z.S., K.S., X.L., N.G. and D.N. wrote the manuscript. All authors contributed to discussions and revisions of the manuscript.

Competing interests

The authors declare no competing interests.

Additional information

Supplementary information is available for this paper at https://doi.org/10.1038/s41592-019-0651-0.

Correspondence and requests for materials should be addressed to D.N.

Peer review information Allison Doerr was the primary editor on this article and managed its editorial process and peer review in collaboration with the rest of the editorial team.

Reprints and permissions information is available at www.nature.com/reprints.

nature methods

SUPPLEMENTARY INFORMATION

https://doi.org/10.1038/s41592-019-0651-0

In the format provided by the authors and unedited.

In situ structure determination at nanometer resolution using TYGRESS

Kangkang Song[1,3,5], Zhiguo Shang[1,5], Xiaofeng Fu[1,4,5], Xiaochu Lou[1,5], Nikolaus Grigorieff[2] and Daniela Nicastro[1]*

[1]Departments of Cell Biology and Biophysics, University of Texas Southwestern Medical Center, Dallas, TX, USA. [2]Janelia Farm Research Campus, Howard Hughes Medical Institute, Ashburn, VA, USA. [3]Present address: Cryo-EM Core Facility, University of Massachusetts Medical School, Worcester, MA, USA. [4]Present address: Biological Science Imaging Resource, Florida State University, Tallahassee, FL, USA. [5]These authors contributed equally: Kangkang Song, Zhiguo Shang. *e-mail: daniela.nicastro@utsouthwestern.edu

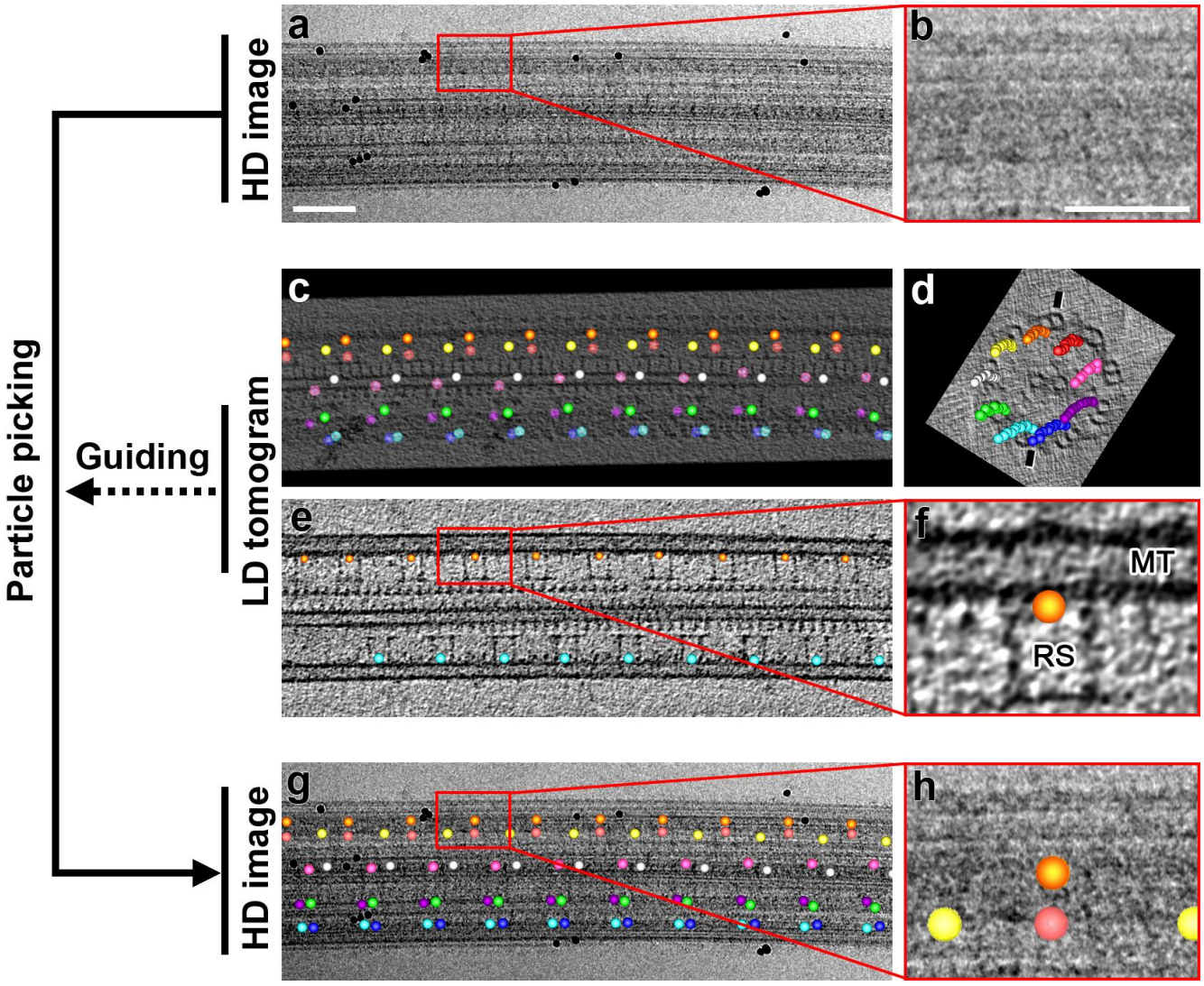

Supplementary Figure 1

Particle picking from HD image, guided by LD-tomogram.

(**a** and **b**) A typical HD image of a single axoneme (**a**) and one of its particles (**b**, a single 96 nm repeat, cut out and zoomed-in from the red box in **a**) show no clear features to enable particle picking because of the overlap of many structures in the projection image. (**c-f**) In the corresponding tomogram slice, many prominent particle features, such as radial spokes and microtubule walls ('RS' and 'MT' in **f**) are well-defined to help pick repeating particles (orange dot in **f**) in 3D (red box area in **e**). In (**c** and **d**) the locations for all picked particles are shown as colored dots. Each color represents one of the 9 DMTs. (**g** and **h**) After the conversion of 3D coordinates into 2D, all particles can be picked on the HD image (**g**); the particle shown in (**f**) is centered at the upper orange dot (**h**). Scale bars: 100 nm (**a**, **c**, **e**, and **g**); 50 nm (**b**, **f**, and **h**).

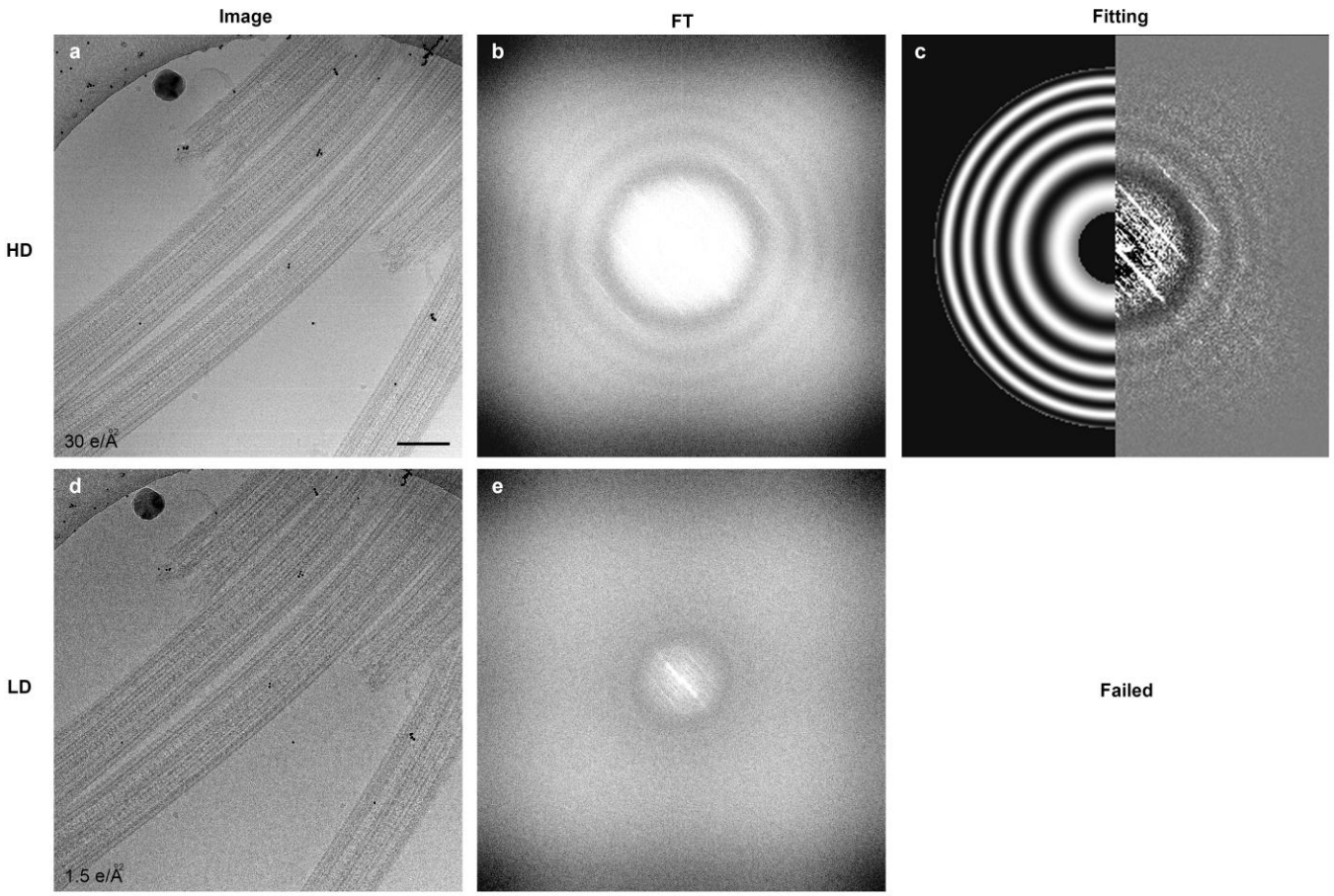

Supplementary Figure 2

The determination of the defocus value succeeded for TYGRESS HD images but failed for regular cryo-ET LD images.

(**a-c**) An HD image of *Tetrahymena thermophila* axonemes recorded at 0° tilt with a defocus setting of -2.5µm (**a**), its Fourier transform (FT) (**b**), and its averaged power spectrum (**c**, right), fitting to the theoretical Thon rings (**c**, left). (**d-e**) A corresponding LD image (0° tilt, defocus setting -8µm) (**d**) and its Fourier transform (**e**). The electron dose of each image is indicated in the bottom left corner of the images. Strong layer lines diffracted from the repeating structures of the axoneme and dark Thon rings (indicated by dashed lines) are visible in the HD image (**b**) but not in the LD image of the same sample (**d** and **e**). This causes the defocus detection to fail for the LD image. Scale bar: 200 nm.

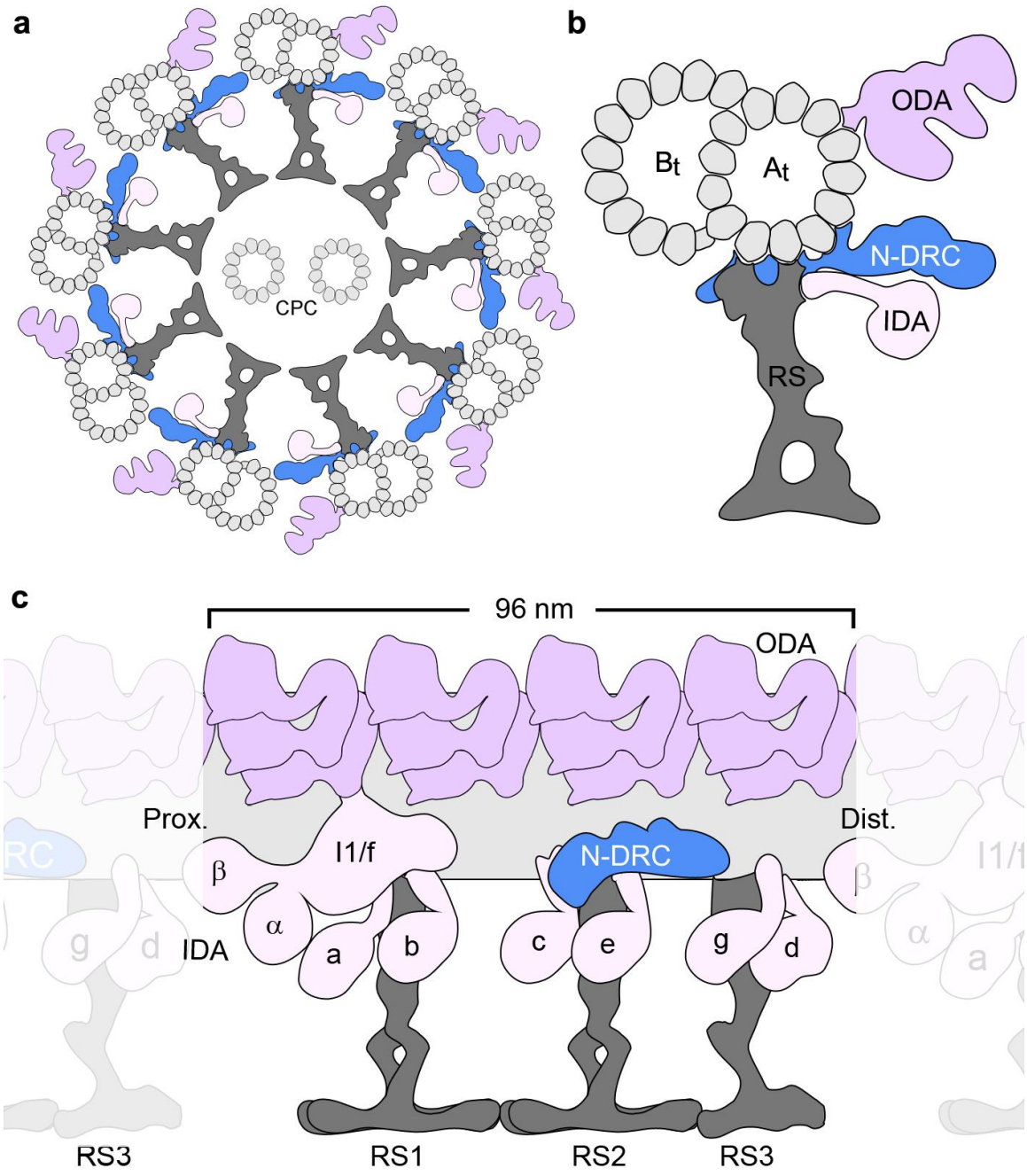

Supplementary Figure 3

Schematic diagram of the axoneme structure.

(**a-c**) Diagrams of intact axoneme (**a**) and a selected DMT with associated complexes (**b**) viewed in cross-section (viewed from proximal). The nexin-dynein regulatory complex (N-DRC) links neighboring DMTs. (**c**) A longitudinal diagram of a 96-nm-long axonemal unit that repeats along the DMT; each repeat unit contains four outer dynein arms (ODAs), six single-headed inner dynein arms (IDAs: a, b, c, d, e and g), and one double-headed IDA (I1 or dynein f) anchored to the A-tubule (A_t). Other labels: B-tubule (B_t), central pair complex (CPC), and radial spokes (RSs 1-3); microtubule polarity from proximal to distal.

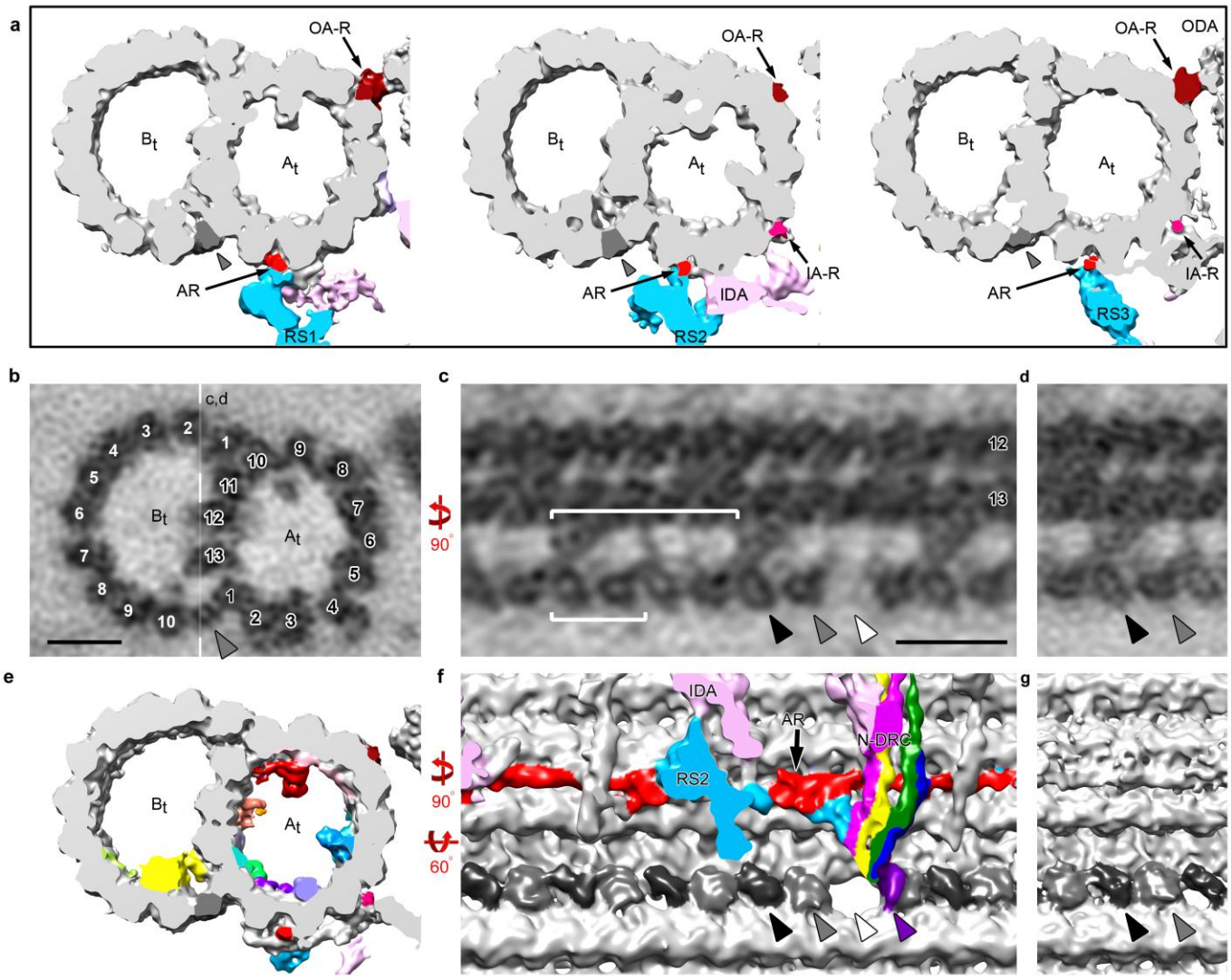

Supplementary Figure 4

Filamentous structures outside the DMT and the inner junction (IJ).

(**a**) Cross-sectional slices of isosurface renderings of the 96-nm axonemal repeat at three different locations showing the locations of the ODA ruler-like structure (OA-R, dark red), 96-nm axonemal ruler (AR, red), and the IDA ruler-like structure (IA-R, magenta), as well as their interactions between radial spokes (RS1-3, light blue) and inner dynein arms (IDA, rose). (**b**-**g**) EM slices (**b**-**d**) and 3D isosurface renderings (**e**-**g**) of the TYGRESS reconstructed 96-nm axonemal repeat (**b**, **c**, **e** and **f**) and a 16-nm DMT repeat (**d** and **g**) show e.g. the inner junction (IJ) that consists of FAP20 (gray arrowheads and coloring) and PACRG (black arrowheads and coloring) that repeat with 8 nm periodicity, whereas their connections with protofilament A13 have a 16 nm periodicity (as indicated in **c**), as well as an additional density extending from the N-DRC baseplate (purple arrowheads and coloring). The white line in (**b**) indicates the location of the EM slices shown in (**c** and **d**). The microtubule protofilaments numbers of the A- and B-tubules are labelled with black and white numbers in (**b** and **c**), respectively. The hole in the IJ is indicated by white arrowheads. The MAPs and MIPs in (**e** and **f**) are colored according to the coloring used in Figures 3 and 4. Scale bars: 10 nm.

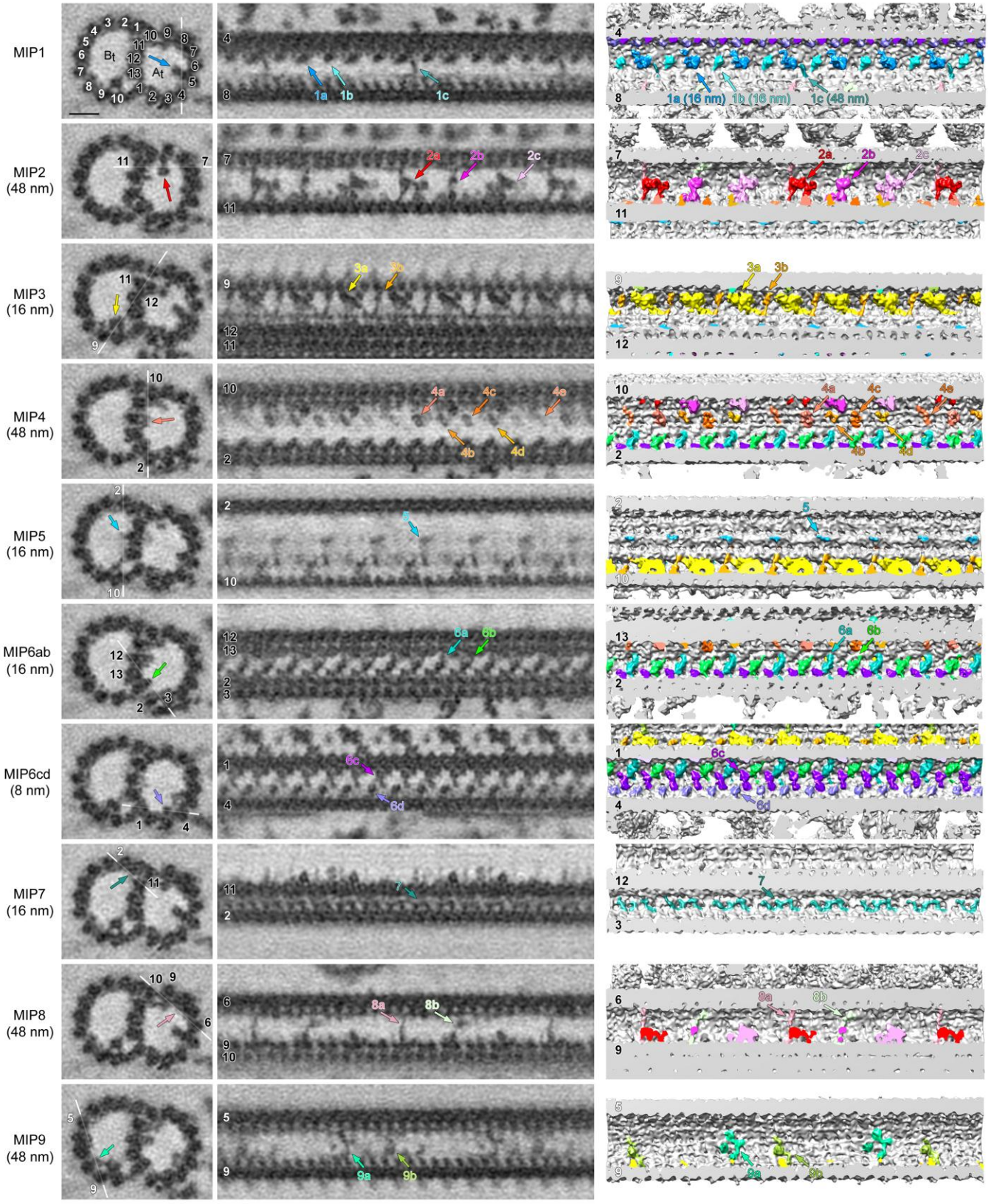

Supplementary Figure 5

Structural characteristics of MIPs 1-9 in intact axonemes resolved using TYGRESS.

Cross-sectional (left column) and longitudinal (middle column) EM slices, and longitudinal views of 3D isosurface renderings (right column) of the 96-nm axonemal repeat show MIPs 1-9. The MIPs are colored and numbered according to their locations in the cross-section (see **Fig. 4d**,**e**). MIPs present at similar locations in the cross-sectional view but in various locations in longitudinal views are further distinguished by letters (a-e). MIP periodicities are indicated by numbers in brackets on the left. White lines in the cross-sections indicate the locations of the EM slices shown in the middle column. The protofilament numbers of the A- and B-tubules are indicated by black and white labels, respectively. Scale bars: 10 nm.

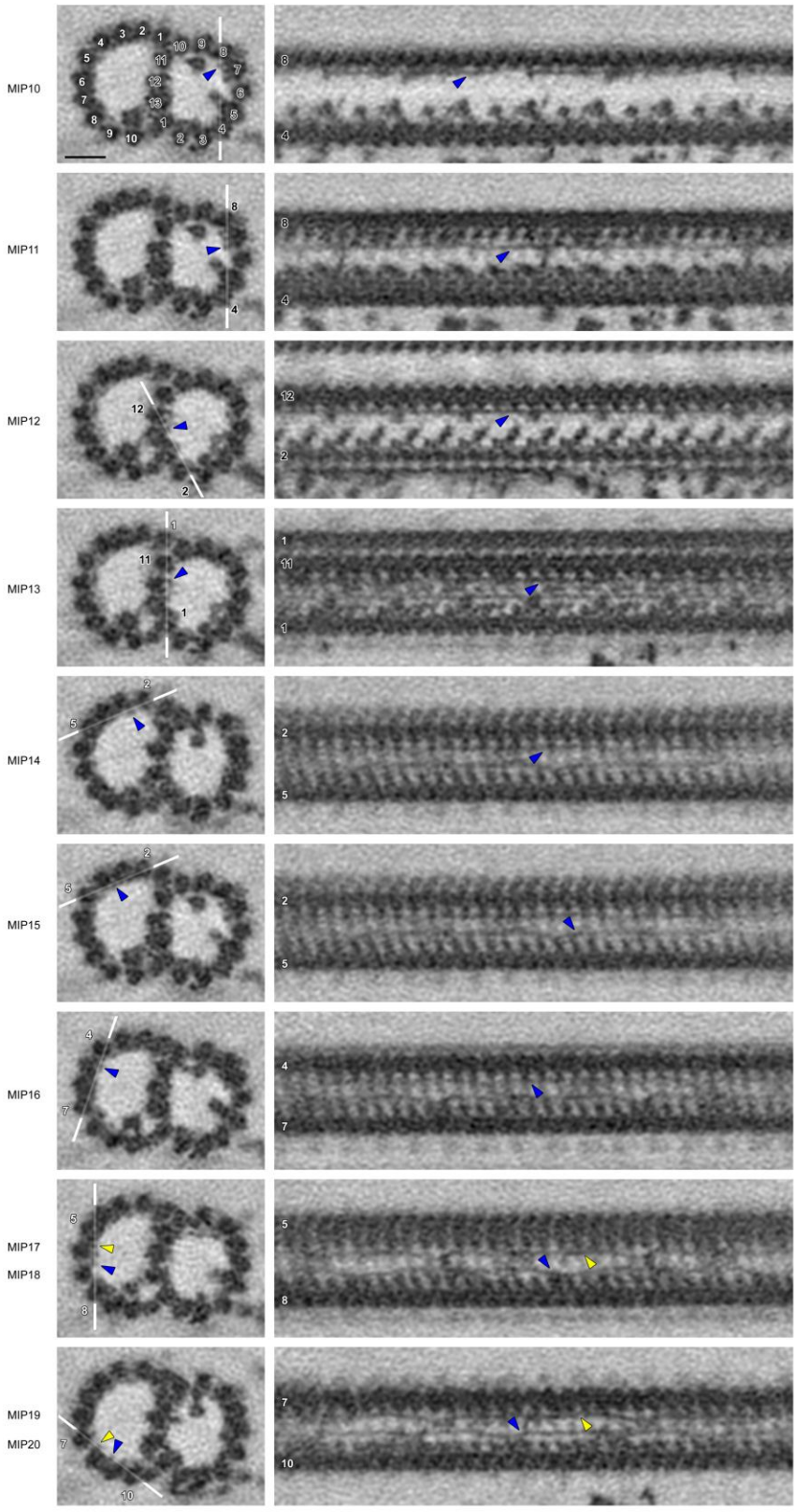

Supplementary Figure 6

Filamentous MIPs in intact axonemes resolved using TYGRESS.

Cross-sectional (left column) and longitudinal (middle column) EM slices of the 96-nm axonemal repeat show the eleven resolved filamentous MIPs. The protofilament numbers of the A- and B-tubules are indicated by black and white labels, respectively. The dark blue arrows highlight the corresponding MIPs. White lines in the cross-sections show the locations of the corresponding longitudinal EM slices. Scale bars: 10 nm.

Supplementary Table 1. Comparison of factors that limit the resolution of cellular cryo-ET and single-particle cryo-EM

Factor	Single particle cryo-EM	Cellular cryo-ET	desired
Specimen thickness	20-100 nm (only viruses more)	100-300 nm	low
Electron dose/sample*	15-30 e/Å^2	80-120 e/Å^2	low
Electron dose/image	15-30 e/Å^2	1-2 e/Å^2	high
# of images/average	20 k-100 k	100/tilt series x 1000 = 100 k	high
Dose/average	50 k x 20 e/Å^2 => 1 Mill e/Å^2	100 x 1 k x 1 e/Å^2 => 100 k e/Å^2	high
# of alignment steps	1 time (particle)	2 times (global tilt series + particle)	low
Defocus	1-3 µm	6-10 µm	low
Tilt	0°	0°-60°	low
Ability of CTF correction	Yes	Challenging	

Note: 'desired' stands for when the parameter results in high resolution structures.
*) Since dose weighting was introduced [Grant, T., Grigorieff, N., Measuring the optimal exposure for single particle cryo-EM using a 2.6 A reconstruction of rotavirus VP6. *eLife* **4**, e06980 (2015).], the dose per image has increased (up to ~100 e/Å^2), but the high-frequency information is only used from frames with low electron dose exposure.

Supplementary Table 2. K2 parameters setup for TYGRESS

Parameters	HD image	LD images
Mode	Super-resolution/movie	Counting/movie
Movie setup	Total exposure time 40 s, 0.5 s/frame	Total exposure time 2 s per degree, 0.4 s/frame
Binning	0.5	1
Defocus setup (µm)	1.5 - 3	8
Total dose (e/Å^2)	~ 30	~ 100
Magnification	9400 x	9400 x
Pixel size (Å)	2.112	4.224
Tilt series setup	N/A	1.5 e/Å^2 @ 0°, increment 2°; tilt from 0° to about -64° and from 2° to about 64°
Angle	0°	0° - 64°

User Manual for Tomography-Guided 3D Reconstruction of Subcellular Structures (TYGRESS)

Authors: Zhiguo Shang[1,3], Kangkang Song[1,3,4], Xiaofeng Fu[1,5], Xiaochu Lou[1], Nikolaus Grigorieff[2], Daniela Nicastro[1,*]

Affiliations:
[1]Departments of Cell Biology and Biophysics, University of Texas Southwestern Medical Center, Dallas, TX 75390, USA.
[2]Janelia Farm Research Campus, Howard Hughes Medical Institute, 19700 Helix Drive, Ashburn, VA 20147, USA.
[3]These authors contributed equally to this work.
[4]Current address: Cryo-EM Core Facility, University of Massachusetts Medical School, Worcester, MA 01655.
[5]Current address: Biological Science Imaging Resource, Florida State University, Tallahassee, FL 32306.

*Correspondence to: Daniela Nicastro, Phone: (++ 1) 214 648 3925; Fax: (++ 1) 214 648 7491; E-mail: daniela.nicastro@utsouthwestern.edu.

Abstract
Recent advances in cryo-electron microscopy (cryo-EM) are paving the way to determining isolated three-dimensional (3D) macromolecular structures at near-atomic resolution using single-particle cryo-electron microscopy (SP-cryo-EM). However, determining the subcellular structures in intact cells and organelles using cryo-electron tomography (cryo-ET) and subtomogram averaging, another cryo-EM technique, with comparable resolution remains a challenge. Current methodologies can only reach a resolution of several nanometers in most samples studied. Here, we introduce a new hybrid method, called Tomography-Guided 3D Reconstruction of Subcellular Structures (TYGRESS) that is able to achieve structural determination of subcellular structures within their natural crowded environment with nanometer-resolution by combining the advantages of cryo-ET and SP-cryo-EM.

Introduction

SP-cryo-EM and cryo-ET both generate three-dimensional (3D) reconstructions of native biological macromolecules under cryogenic conditions. However, whereas SP-cryo-EM can be used to determine the structure of isolated macromolecules with up to atomic resolution (~3Å), the resolution achieved by cryo-ET of intact cells or organelles paired with subtomogram averaging lags approximately one order of magnitude behind (~30Å). Here, we introduce a hybrid-method called "TomographY-Guided 3D REconstruction of Subcellular Structures" (TYGRESS), which combines the advantages of both SP-cryo-EM (images with good signal-to-noise ratio/contrast and minimal radiation damage of the sample) and cryo-ET averaging (extraction and 3D alignment of macromolecules contained in a complex cellular sample). Ultimately TYGRESS is a SP-reconstruction, but the parameters from subtomogram averaging are critical to guide particle picking and image alignment – steps that usually prohibit SP-cryo-EM of complex cellular samples.

In this method, a typical high dose (HD) single particle cryo-EM micrograph is acquired (i.e., with an electron dose that is higher than for individual tile series images) immediately prior to a conventional low dose (LD) cryo-ET tilt series. The LD cryo-ET data set are processed, including subtomogram averaging of the particle of interest. The parameters, i.e., the particle position and alignment, are then used to guide the particle picking in the HD single-particle cryo-EM data set and initialize its angular alignment. With this information from cryo-ET, single particle image processing techniques can be applied to subcellular samples, despite the superposition of many structures in the SP projection image.

Equipment

Hardware requirements and software installation

A computer cluster and/or workstation with GPU with shared storage is recommended for running TYGRESS. Before installation of TYGRESS, please ensure the software packages below are installed by following the installation guide of each package. You can also find the hardware and operating system requirements in the distribution pages of the following software packages.

MATLAB: The major running environment for TYGRESS. Use the R2014b version of MATLAB for the best results.
IMOD & **PEET**: Tilt series alignment, tomogram generation, and subtomogram averaging. (http://bio3d.colorado.edu/imod/ & http://bio3d.colorado.edu/PEET/)
CTFFIND3: Detect defocus value (http://grigoriefflab.janelia.org/ctf)
EMAN2: 'Normalization' function (https://blake.bcm.edu/emanwiki/EMAN2)
FREALIGN: 3D reconstruction (http://grigoriefflab.janelia.org/frealign)
Bfactor: Apply B-factor for the final reconstruction (http://grigoriefflab.janelia.org/grigorieff/download_b.html)

Procedure

1: Preparation to run TYGRESS

1.1 To use TYGRESS on the example data set, download and unzip the TYGRESS source code and example data set package (www.tygress.org), and then follow Procedure step 2 ("Preparation of TYGRESS input files" below).
Note: TYGRESS is also available on Code Ocean as a compute capsule (*Linkage and DOI will be available after the manuscript is accepted for publication*). Please read the readme file on the Code Ocean TYGRESS page for more details.

1.2 To use your own data set, please finish the data collection, tomogram reconstruction, and subtomogram averaging before following Procedure 2, below.

1.2.1 **Data collection**. During data collection, two data sets need to be acquired for each region of interest. (1) First, acquire a 2D image at 0 degree using an electron dose typical for conventional SP-cryo-EM (HD image), which is used for final TYGRESS reconstruction; (2), immediately after collecting the HD image, collect a traditional low-dose tilt series (LD images) of the same region, which is used for retrieving the position information for each particle of interest after tomogram reconstruction and subtomogram averaging. Note: to minimize the effects of radiation damage in the final reconstruction, the HD image must be recorded prior to the LD images.

1.2.2 **Motion correction**. If movie stacks were taken during the data collection, run the whole-frame motion correction using IMOD scripts.

1.2.3 **Alignment of the combined tilt series**. Each HD image needs to be inserted into its corresponding tilt series at the angle where the HD image was taken using the "newstack" command in the IMOD package, resulting in a "combined tilt series". For example, an HD image recorded at 0 degrees should be inserted just before the LD image at 0 degrees. After tilt series alignment using the IMOD package, the combined HD and LD images ensure a common reference frame for the later steps in the TYGRESS procedure.

1.2.4 **Tomogram reconstruction**. After alignment, only the LD images are used to generate the tomogram using the IMOD package.

1.2.5 **Subtomogram averaging**. The subtomogram averaging can be performed using the PEET package in IMOD. Run PEET averaging for each tilt series and all of the particles of interest, respectively.

2: Preparation TYGRESS input files.

2.1 Prepare two TYGRESS input text files.

2.1.1 There is one file named as "TYGRESS_input.txt" in the TYRESS source code folder (as shown below in the example data set), which contains all the parameters to run TYGRESS, such as the work directory, file path, 3D reconstruction parameters, *etc*. Update these parameters as needed to reflect the location and organization of your files. If you are following along with the example dataset, modify the following:

- fnDataDir= (copy the full path name for the example data folder that you downloaded from this tutorial)
- fncode= (copy the full path name for the TYGRESS source code folder that you downloaded from this tutorial)
- fnref= (copy the full path name for the .mrc file within the example folder)

Example of a “TYGRESS_input.txt” file

==========

Part I Parameters for running TYGRESS

fnDataDir =	/project/cellbiology/Nicastro_lab/nusr/shang/linux/Tygress/example/	% project data directory
fncode =	/home2/s165838/Tygress/Tcoden/Tcode/	% TYGRESS code directory
fnWorkDir =	combined_PEET/	% combined peet directory
fnDef =	ctffind/DefocusList.txt	% defocus file
fnref =	/home2/s165838/Tygress/ref.mrc	% reference masked after PEET average
fnCombinedHD =	HD_particles/	% high dose 2D particle directory
fnmod =	combined_mod_csv/	% combined mod & csv directory
fncsv =	Iter1_particles/	% updated peet run for whole dataset
csvDirname =	Itr1/	% csv directory
csvname_h =	_Itr1_MOTL_Tom	% csv root name after PEET of individual tilt series
csvname_t =	_Iter5.csv	% csv tail name after PEET of individual tilt series
modname_h =	A1.mod.FOIE.	% mod root name after PEET of individual tilt series
modname_t =	.txt.mod.txt.Ax_Pred_.txt.mod	% mod tail name after PEET of individual tilt series
fnPEETRoot =	example	% root name for PEET running
particleSize =	180	% particle size for PEET running
fnDist =	N	% file for correct distortion (gif camera), 'N' for no correction
tail_st =	_fused.st	% entire tilt date set
tail_hd =	_HD.st	% file name use for save HD micrograph
amplitude_contrast =	0.14	% thin ice sample use 0.07 and thick ice use 0.14
axoRepeat =	180	% pixel size for particle (used for remove edged particles) in high dose micrograph
Mag1 =	22500	% micrograph magnification
PickSize =	300	% size for pick 2D high dose particle
sizex =	200	% size for final out put structure
root_csv =	_MOTL_Tom	% csv root name after run entire PEET
tail_csv =	_Iter2.csv	% csv tail name after run entire PEET
SizeRef =	180	% size of reference volume
sx =	4	% shift range of coordinates, nm
sa =	2	% shift range of orientation, degree
parallel_f =	1	% set 1 for run job in parallel job
Ncpu =	5	% cup number for parallel job
tail_rec =	_fused_exHD.rec	% tail part of rec file
pixel_size =	5.562	% angstrom per pixel for raw particle
kV =	300	% voltage
Cs =	2	% value of spherical aberration coefficient of objective in mm
use_ctf =	1	% set 1 for ctf correction
out_mrc =	96nm	% output reconstruction file
imageSize =	2048	% entire raw image size K*K
sizescale =	0.6	
n_neighbor =	2	% number of neighbored particles which used for background reference
dis_neighbor =	90	% distance (# pixels) used for selecting nearby particles for background reference

Part II Parameter file for reconstruction, visit FREALIGN webpage for more details

data_input	96nm
raw_images1	96nm
thresh_reconst	90.0
thresh_refine	90.0
pixel_size	5.562
dstep_frealign	13
WGH	0.14
kV1	300.0
Cs	2.0
RI	0.0
RO	3000.0

PBC	2.0
BOFF	75.0
ASYM	0
DANG	1
ITMAX	10
MODE	1
XSTD	0.0
RBFACT	0
FPART	F
FMAG	F
FDEF	F
FASTIG	F
IEWALD	0
dfsig	100
FBEAUT	F
FCREF	F
res_reconstruction	3.0
res_low_refinement	800.0
res_refinement	3.0
start_process	1
end_process	1
first_particle	1
last_particle	471
increment	10

==========

Note: When modifying the "TYGRESS_input.txt" file, please use the full path name to the directories for 'fnDataDir', 'fncode', and 'fnref', and only use the relative file folder names for the other parameters when needed.

2.1.2 The file named "DataList.txt" in the TYGRESS source code folder (as shown below in the example data set) has three columns containing the "data set main name" + "data set sub name" + "total .mod number", which you should change as needed.

Example of a "DataList.txt" file

```
==========================================================================
WT_20120914   S1   9
WT_20120914   S2   9
WT_20120914   S3   9
WT_20120914   S4   9
WT_20120914   S5   9
==========================================================================
```

2.2 Modify the "ctffind.csh" file in the TYGRESS source code folder, which will be used to determine CTF. Please see the example in the "ctffind.csh" file for details. You may at least need to change the path of the "ctffind3.exe" file. For more details about how to modify this file, please visit (http://grigoriefflab.janelia.org/sites/default/files/readme_ctf.txt).

2.3 Modify the path of your FREALIGN installation in the "mreconstruct_noMask.com" file. Please see the example "mreconstruct_noMask.com" file for details.

3: Run TYGRESS

Open the Matlab interface, and set the TYGRESS source code folder as the work path. Then, in Matlab, open the TYGRESS_GUI (Figure 1). Click the "Tygress parameter file" button, input the "TYGRESS_input.txt" file, click the "Data list" button, and input the "DataList.txt" file. Click "Yes" on the corresponding step to have TYGRESS run that step (Figure 1). All steps should be run in order if it is your first time processing your TYGRESS data. (Note: You can process the steps one by one, or you can run all selected steps together.)

Final 3D reconstruction is performed with FREALIGN, and all output is saved under the "Reconstruction" folder. For more information about FREALIGN, please visit (http://grigoriefflab.janelia.org/frealign).

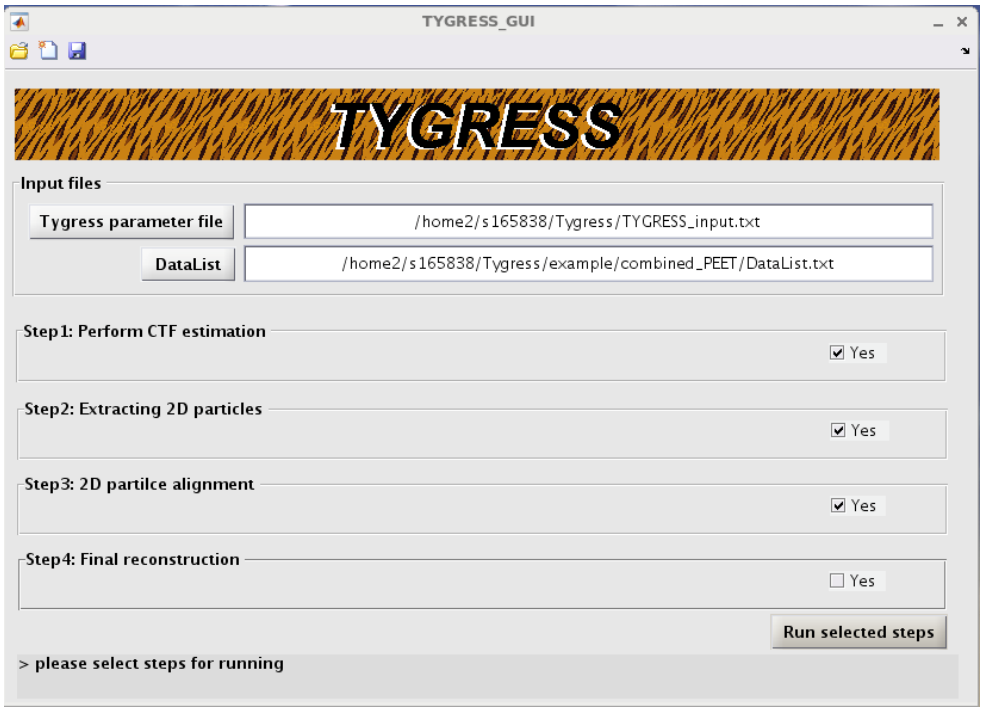

Figure 1: Example of TYGRESS GUI

4: Directory tree of TYGRESS

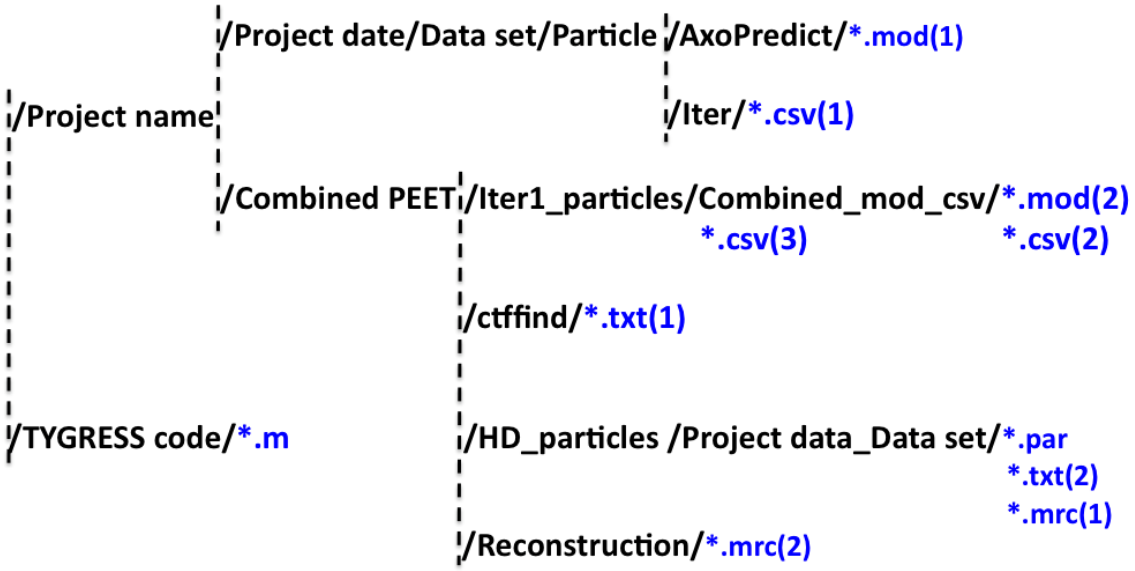

Figure 2: Work directory tree of TYGRESS

Please note:

- .mod(1) and .csv(1) are the parameters after running PEET for individual tilt series
- .mod(2) and .csv(2) are the parameters for running PEET for the entire data, and .csv(3) is the output
- .csv(3) and mod(2) are used for TYGRESS alignment and to generate the .par file
- .mrc(1) is the 2D particle data set and .mrc(2) is the final output for the 3D structure
- .txt(1) is the parameter for defocus and .txt(2) coordinates parameters of each particle
- .m is the code for running TYGRESS
- **Project data** folder contains all tilt series data; each tilt series is processed (alignment and reconstruction in IMOD) in its own particles folder, including particles_Predict and Iter folders (alignment results from individual PEET runs).
- **Combined_PEET** folder includes combined alignment for all 3D subtomogram particles in PEET (Iter1_particles); Combined_mod_csv contains the file for running PEET for the entire dataset; 2D HD particles are picked in each data set under the HD_particles folder. The defocus detection for HD images is put in the ctffind folder.
- **TYGRESS code** folder stores all codes needed for running TYGRESS. The 'm'extension indicates matlab scripts, which can be only executed in Matlab. The structure is output as a .mrc file.
- **Reconstruction** folder stores all output results after reconstruction with FREALIGN.

5: Anticipated Results

5.1 *.mod(1) and *.csv(1) are the output files after running PEET for each individual tilt series.

5.2 You can copy the *.mod(1) and *.csv(1) to the Combined_mod_csv folder as *.mod(2) and *.csv(2) to run the PEET for the whole datasets, and then you will get *.csv(3) after PEET. All these .mod and .csv files are obtained before you starting to run TYGRESS.

5.3 After you run **Step 1** in the TYGRESS GUI, the “ctffind” folder will be created and the defocus information will be saved in the *.txt(1) file. Moreover, the “HD_particle” folder will be created and all HD images will be saved in its sub_folder.

5.4 After you run **Step 2** in the TYGRESS GUI, the program will use the information from *.mod(2) and *.csv(3) to pick particles from the HD images, and then save all picked 2D particles as *.mrc file and save the coordinate parameters of each picked particle as *.txt(2) file, and alignment parameters as *.par file.

5.5 After you run **Step 3** in the TYGRESS GUI, the program will align the 2D particles picked and update the *.par file. **Note:** for further constrained alignment, you need to update your 'sx' (for x, y shift) and 'sa' (for angular shift) values in the “TYGRESS_input.txt” file, use the *.par file created in **Step 3** to replace the *.par file generated in **Step 2,** and re-run **Step 3**.

5.6 After you run **Step 4** in the TYGRESS GUI, the program will generate the 3D reconstruction and save the *.mrc(2) file.

6: Timing

In the example data set, which includes five tilt series, each tilt series includes all the files generated after tomogram reconstruction and subtomogram averaging. The PEET averaging for the whole dataset is also included. Therefore, you can run TYGRESS directly after changing the work directories in the “TYGRESS_input.txt” file. The total TYGRESS processing time from CTF finding to final reconstruction will take less than 30 minutes on a common computer cluster.

7: Associated Publications

This protocol is related to the following article:

Song, K., Shang, Z., Fu, X., Lou, X., Grigorieff, N., and Nicastro, D. (2018). Structure of the ciliary axoneme at nanometer resolution reconstructed by TYGRESS. *BioRxiv* 363317.

8: Competing financial interests

The authors declare no competing financial interests.